Monthly Notices of the ROYAL ASTRONOMICAL SOCIETY

MNRAS **508,** 4412–4428 (2021) https://doi.org/10.1093/mnras/stab1619
Advance Access publication 2021 June 07

A precise photometric ratio via laser excitation of the sodium layer – II. Two-photon excitation using lasers detuned from 589.16 and 819.71 nm resonances

Justin E. Albert [1★] Dmitry Budker [2,3,4] Kelly Chance [5] Iouli E. Gordon [5] Felipe Pedreros Bustos [2,6] Maxim Pospelov,[1,7,8] Simon M. Rochester [3] and H. R. Sadeghpour [5]

[1]*Department of Physics and Astronomy, University of Victoria, Victoria, British Columbia V8W 3P6, Canada*
[2]*Helmholtz Institute, Johannes Gutenberg-Universität Mainz, D-55099 Mainz, Germany*
[3]*Rochester Scientific LLC, El Cerrito, CA 94530, USA*
[4]*Department of Physics, University of California, Berkeley, CA 94720, USA*
[5]*Harvard-Smithsonian Center for Astrophysics, Cambridge, MA 02138, USA*
[6]*Laboratoire d'Astrophysique de Marseille (LAM), Université d'Aix-Marseille & CNRS, F-13388 Marseille, France*
[7]*Perimeter Institute of Theoretical Physics, Waterloo, Ontario N2L 2Y5, Canada*
[8]*Now at School of Physics and Astronomy, University of Minnesota, Minneapolis, MN 55455, USA*

Accepted 2021 May 31. Received 2021 May 20; in original form 2021 January 18

ABSTRACT

This paper is the second in a pair of papers on the topic of the generation of a two-colour artificial star [which we term a laser photometric ratio star (LPRS)] of de-excitation light from neutral sodium atoms in the mesosphere, for use in precision telescopic measurements in astronomy and atmospheric physics, and more specifically for the calibration of measurements of dark energy using type Ia supernovae. The two techniques, respectively, described in both this and the previous paper would each generate an LPRS with a precisely 1:1 ratio of yellow (589/590 nm) photons to near-infrared (819/820 nm) photons produced in the mesosphere. Both techniques would provide novel mechanisms for establishing a spectrophotometric calibration ratio of unprecedented precision, from above most of Earth's atmosphere, for upcoming telescopic observations across astronomy and atmospheric physics; thus greatly improving the performance of upcoming measurements of dark energy parameters using type Ia supernovae. The technique described in this paper has the advantage of producing a much brighter (specifically, brighter by approximately a factor of 10^3) LPRS, using lower power ($\lesssim$30 W average power) lasers, than the technique using a single 500 W average power laser described in the first paper of this pair. However, the technique described here would require polarization filters to be installed into the telescope camera in order to sufficiently remove laser atmospheric Rayleigh backscatter from telescope images, whereas the technique described in the first paper would only require more typical wavelength filters in order to sufficiently remove laser Rayleigh backscatter.

Key words: instrumentation: miscellaneous – methods: observational – techniques: photometric – telescopes – dark energy.

1 INTRODUCTION

The motivations for the generation of a laser photometric ratio star (LPRS) are detailed in the first paper in this pair of papers (Albert et al. 2021, hereafter referred to as Paper I). To briefly review: measurements of dark energy using type Ia supernovae (SNeIa) are limited by systematic uncertainty on astronomical magnitude as a function of colour, within the optical spectrum (Wood-Vasey et al. 2007; Betoule et al. 2014; Jones et al. 2018); the generation of an LPRS above an SNeIa-survey telescope could provide a precise calibration source to effectively eliminate this dominant uncertainty. Additionally, other types of astronomical measurements (besides SNeIa cosmology) could greatly benefit from reduction in relative photometric uncertainty (Kirk et al. 2015; Connor et al. 2017) via LPRS-based calibration. In this paper, we detail a technique for the generation of an LPRS that utilizes two lasers, at optical frequencies that are, respectively, approximately 3.9 GHz below and above neutral sodium atomic resonances that occur at wavelengths of 589.16 and 819.71 nm.[1] As we will show, this technique for LPRS generation will result in a significantly brighter LPRS with an apparent magnitude of approximately 12 (as compared with magnitude 20), using much lower power lasers, than the technique described in Paper I.

★ E-mail: jalbert@uvic.ca
Present address: School of Physics and Astronomy, University of Minnesota, Minneapolis, MN 55455, USA.

[1]In this paper, wavelengths are given in vacuum, typically to either the nearest nanometre, or nearest hundredth of a nanometre. Wavelengths for sodium are as provided by Kelleher & Podobedova (2008).

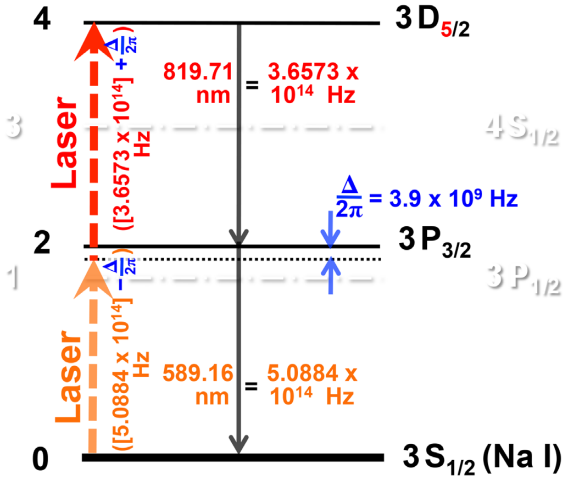

Figure 1. Atomic level diagram (not to scale) for neutral sodium atoms in the two-laser LPRS technique described in this paper. The allowed transitions and levels (i.e. levels 0, 2, and 4 in the diagram) are in solid black, whereas a dotted black line represents the off-resonant energy corresponding to the frequency of the first laser. The 5 in the allowed $3\,D_{5/2}$ level is red to distinguish this atomic state from the $3\,D_{3/2}$ Na I state that is excited by the 343 nm laser in the technique described in Paper I. The two 'ghost' levels (1 and 3) below the $3\,D_{5/2}$ excited state, that are both inaccessible from states in the diagrams that are excited by the lasers, are shown in shadowed grey text and dash–dotted lines. As is shown, this LPRS technique results in a 'fully mandated cascade' from the 819.71 nm de-excitation to the 589.16 nm de-excitation, resulting in a mandated 1:1 ratio between those produced photons.

2 LPRS USING TWO LASERS DETUNED FROM NA I ATOMIC RESONANCES

Fig. 1 outlines how neutral sodium atoms (Na I) in the ground state can undergo photoexcitation to the $3\,D_{5/2}$ state via two-photon absorption using pulses from two lasers, with one laser adjusted to a wavelength slightly greater than the Na I resonance at 589.16 nm and the second laser adjusted to a wavelength that is correspondingly smaller than the Na I resonance at 819.71 nm. The value of the selected 'detuning parameter' Δ can be modified: as we show quantitatively below, smaller values of Δ would result in a brighter LPRS. However, if $\frac{\Delta}{2\pi}$ were chosen smaller than approximately 3.3 GHz, then at least 1 per cent of the observed photons from the LPRS Na I de-excitation would result from direct single-photon excitation to the $3\,P_{3/2}$ state rather than from two-photon excitation to the $3\,D_{5/2}$ state, which would serve to spoil the precise 1:1 photometric ratio characteristic of the resulting LPRS. We have, thus, selected a value of $\frac{\Delta}{2\pi} = 3.9$ GHz, so that a smaller fraction than approximately 2 out of 10^5 observed photons from the Na I de-excitation in the LPRS will result from single-photon excitation to the $3\,P_{3/2}$ state, rather than from the intended two-photon excitation to the $3\,D_{5/2}$ state.

2.1 Backgrounds from Rayleigh scattering and from virtual $3\,P^*_{3/2}$ production, and the need for STIRAP

Before providing a formula for the excitation rate of the signal process shown above in Fig. 1 as a function of the detuning parameter and of the two laser intensities, we critically note that, if other laser parameters besides the detuning and intensity (i.e. pulse timings, shapes, and polarizations) were not chosen carefully, there would be two forms of dominant backgrounds to the process: near-180° atmospheric Rayleigh back-scattering of light from the lasers; and the de-excitation of virtual Na I excitations, which we denote as $3\,P^*_{3/2}$ (located near in frequency to the non-virtual $3\,P_{3/2}$ state) that would be excited in the sodium layer during pulses by the 589.16 nm laser. We discuss backgrounds further, and calculate their expected rates, in Section 6 of this paper, but in order to first begin to consider the outline of an optimal system to reject as much background light, but generate and accept as many signal photons, as is possible, we must first consider some basic choices in pulse timings, shapes, and polarizations from the two lasers.

The background from near-180° Rayleigh back-scattering of 589.16 and 819.71 nm light from the two lasers will result in a large flux of photons of those two wavelengths into the telescope aperture. Note that this is a similar issue to the Rayleigh scattering background encountered in Paper I; however, the problem is compounded in the present situation by the fact that here these are nearly the same two wavelengths as the signal photons from the LPRS itself. Thus, in this case one cannot just improve the out-of-band rejection of the telescope filters (as one could in that previous situation where a single 342.78 nm laser was used). The main handle in the present situation for the rejection of Rayleigh back-scattered background photons will, thus, need to be polarization, rather than wavelength. I.e. if the 589.16 nm laser has a given polarization, then the telescope *r* filter (that accepts 589.16 nm light) must *block* that particular polarization, and only accept the orthogonal polarization, thereby blocking a large majority of Rayleigh back-scattered light from that laser. Similarly, if the 819.71 nm laser has a given polarization, then the telescope *i* and *z* filters (that accept 819.71 nm light) must block *that* particular polarization, and only accept the orthogonal polarization. These laser and filter polarizations could, of course, be linear or circular. For a consistent definition of our linear polarization orientations, we define the $\hat{x}$ and $\hat{y}$ orientations to, respectively, be in the east–west and in the north–south geographical directions for the sodium fluorescence light propagating toward the nadir that enters a zenith-pointing telescope and the $+\hat{z}$ direction to always be in the direction of the propagation of the relevant light that is under consideration within

the given context – despite the fact that this Cartesian axis frame of course changes with respect to Earth and the direction of gravity, depending on the light that is under consideration. We shall choose an $\hat{x}$ linear polarization for the light output of the 589.16 nm laser and a $\hat{y}$ linear polarization for the light output of the 819.71 nm laser; and thus the modified telescope r filter must reject $\hat{x}$-polarized light and only accept $\hat{y}$-polarized light, and the modified telescope i and z filters must both reject $\hat{y}$-polarized light and only accept $\hat{x}$-polarized light.

If care were not additionally taken with the laser pulse shapes, and with the relative timing of the pulses of the 589.16 and 819.71 nm lasers (or, for that matter, if either one of the lasers were continuous-wave, rather than pulsed), a large rate of virtual $3\,\mathrm{P}^*_{3/2}$ Na I excitations would occur during the 589.16 nm laser pulses, followed by a decay back down to the ground state and emission of background 589.16 nm light. Specifically, during each 589.16 nm laser pulse, this laser-induced background de-excitation rate (the number of de-excitation events from virtual $3\,\mathrm{P}^*_{3/2}$ excitations per Na I atom per unit time) would be approximately given by

$$W^{\mathrm{Na\,I\,(bkgd.\ de\text{-}excitation\ during\ pulse,\ if\ no\ STIRAP)}}_{(3\,\mathrm{P}^*_{3/2})\,\rightarrow\,(3\,\mathrm{S}_{1/2})+\gamma_{589\,\mathrm{nm}}} \approx \frac{1}{4\hbar^2}\frac{g_k}{g_i}\left[\frac{d_{ik}^2\mathcal{E}_1^2(x,y,t)}{\Delta^2}\right]\Gamma_k, \tag{1}$$

where the detuning parameter Δ was defined previously; states $\{i,k\} \equiv \{3\,\mathrm{S}_{1/2},\ 3\,\mathrm{P}_{3/2}\}$; the level degeneracy ratio $\frac{g_k}{g_i} = \frac{4}{2} = 2$; the natural linewidth Γ_k of state k is $6.16 \times 10^7\ \mathrm{s}^{-1}$; the dipole moment $d_{ik} = \sqrt{\frac{3\epsilon_0 hc^3 A_{ki}}{2\omega_{ki}^3}} = 2.11 \times 10^{-29}$ coulomb-metres (where the Einstein A coefficient $A_{ki} = 6.16 \times 10^7\ \mathrm{s}^{-1}$); and the average electric field strength due to the 589.16 nm laser beam as a function of the transverse distances (x, y) from the beam centreline[2] and the time t after the passage of the mid-point between a given pair of pulses from the two lasers, $\mathcal{E}_1(x, y, t)$, is provided in $\mathrm{V\ m}^{-1}$ within the altitude range of the sodium layer (Budker, Kimball & DeMille 2008). This *nominal* de-excitation rate for virtual $3\,\mathrm{P}^*_{3/2}$ excitations, and resulting background, is larger than our signal excitation rate. However, the use of the laser optical technique known as STIRAP [STImulated Raman Adiabatic Passage; Gaubatz et al. 1990] will allow one to nearly completely avoid the production of virtual $3\,\mathrm{P}^*_{3/2}$ Na I excitations and thus of their associated background de-excitation light.

The STIRAP technique [reviewed by Vitanov et al. (2017)], as specifically considered here, involves pulsing the 819.71 nm laser and then the 589.16 nm laser in succession, such that Na I atoms in the $3\,\mathrm{S}_{1/2}$ ground state are adiabatically transferred by two photons up to the $3\,\mathrm{D}_{5/2}$ state, without ever landing in the intermediate virtual $3\,\mathrm{P}^*_{3/2}$ excitation. In practice, with (for example) pulses from the 819.71 nm laser and the 589.16 nm laser that are each temporally Gaussian-distributed with $\sigma_t^{819.71\ \mathrm{nm}} = \sigma_t^{589.16\ \mathrm{nm}} = 1$ ns, this would involve delaying the Gaussian peak of each 589.16 nm laser pulse to approximately $\sqrt{2}$ ns *after* the peak of each 819.71 nm laser pulse. (We importantly note that this ordering is, at least at first glance, counter-intuitive: the laser at the frequency that is near to the excitation frequency from the ground state to the intermediate state should peak in time *following* the peak of the other laser.) The STIRAP technique has been experimentally demonstrated in many laboratory results since 1990 to have adiabatic transfer efficiencies of nearly 100 per cent, and also to be robust to small experimental variations in laser parameters (Bergmann, Vitanov & Shore 2015). STIRAP has been performed at gas pressures up to atmospheric pressure at sea level [on sodium atoms within an argon buffer gas, Johnson et al. (2010)]; however, STIRAP has not yet been demonstrated in the open atmosphere.

2.2 Effective signal excitation rate

The condition that must be satisfied in order for STIRAP excitations of ground state Na I atoms to the $3\,\mathrm{D}_{5/2}$ excited state to occur, due to a given single pair of pulses from the two lasers, at locations that are a transverse distance[2] (x, y) from the centreline of the laser beams, is

$$\mathcal{A}(x,y) \equiv \frac{1}{\hbar}\int_{-\infty}^{\infty}\left(\sqrt{d_{ik}^2\mathcal{E}_1^2(x,y,t)\ +\ d_{kf}^2\mathcal{E}_2^2(x,y,t)}\right)\mathrm{d}t \quad \gg \quad \frac{\pi}{2}\,, \tag{2}$$

where d_{ik}, $\mathcal{E}_1$, and states i and k are as defined previously; state $f \equiv 3\,\mathrm{D}_{5/2}$; $d_{kf} = \sqrt{\frac{3\epsilon_0 hc^3 A_{fk}}{2\omega_{fk}^3}} = 3.17 \times 10^{-29}$ coulomb-metres (where the Einstein A coefficient $A_{fk} = 5.14 \times 10^7\ \mathrm{s}^{-1}$); and the average electric field strength $\mathcal{E}_2$ due to the 819.71 nm laser beam as a function of (x, y) and of the time t after the passage of the mid-point between a given pair of pulses from the two lasers is provided in V/m within the altitude range of the sodium layer (Vitanov et al. 2017). The quantity $\mathcal{A}$, a function of x and y, is known as the 'pulse area,' although one should note that the values of $\mathcal{A}(x, y)$ itself are dimensionless, rather than having dimensions of area. The condition $\mathcal{A} \gtrsim 10$ is generally sufficient for efficient STIRAP population transfer in laboratory measurements.

The condition in equation (2) will result in a column of sodium atoms through the sodium layer being excited to the $3\,\mathrm{D}_{5/2}$ state each time that a pair of pulses from the lasers passes by; and, if the time between successive pairs of laser pulses is long compared with the total decay time (i.e. compared with about 40 ns) from $3\,\mathrm{D}_{5/2}$ back down to the $3\,\mathrm{S}_{1/2}$ ground state, the resulting two quantities that are relevant for the effective rate of emission of 819.71 and 589.16 nm photons from the sodium atoms in the mesosphere, which are governed

[2]The small divergence of the laser beams implies that the average electric field strength within the sodium layer will also depend on [in addition to depending on (x, y, t)] the path-length that the beam has taken through the atmosphere; however, we average over that effect in our flux calculations in Sections 5 and 6.

by the parameters of the two utilized lasers, will be (1) the cross-sectional area of the column through the sodium layer for which the condition in equation (2) holds true and (2) the time interval between successive pairs of laser pulses. We will determine those two quantities, and will thus estimate the effective rate of emission of 819.71 and 589.16 nm photons from sodium in the mesosphere as discussed in Section 5.

2.2.1 Doppler shift detuning and signal excitation fraction

However, the important effect on STIRAP signal excitation efficiency from Doppler shifts due to the velocity distribution of the sodium atoms in the mesosphere, and from the linewidths of the lasers, must additionally be considered. Determination of the results of these effects on STIRAP efficiency is non-trivial, and multiple methods by various authors [reviewed in Vitanov et al. (2017)] have been developed for analytic and numerical approximation of the results. If, for a given pair of photons in the mesosphere that are, respectively, from the 589 and the 820 nm lasers, we consider the angular frequency detunings from the peak of the 589.16 and the 819.71 nm resonances to, respectively, be $\Delta_{589\,\mathrm{nm}}$ and $\Delta_{820\,\mathrm{nm}}$, and a given Na I atom in the mesosphere to have a velocity vector $\vec{v}$, then the resulting velocity-dependent angular frequency detuning δ_{eff} from the peak of the two-photon STIRAP resonance will be given by

$$|\delta_{\mathrm{eff}}| = |\Delta_{589\,\mathrm{nm}} - \Delta_{820\,\mathrm{nm}} + (\vec{k}_{589\,\mathrm{nm}} + \vec{k}_{820\,\mathrm{nm}}) \cdot \vec{v}|, \tag{3}$$

where $|\vec{k}_{589\,\mathrm{nm}}| = \frac{2\pi}{\lambda_{589\,\mathrm{nm}}}$ and $|\vec{k}_{820\,\mathrm{nm}}| = \frac{2\pi}{\lambda_{820\,\mathrm{nm}}}$ are the wavevectors of the two respective photons. Thus, in the case of perfectly null two-photon detuning (i.e. when $\Delta_{589\,\mathrm{nm}} = \Delta_{820\,\mathrm{nm}}$) if, for example, the two photons happen to reside at the peaks of the two laser lines, we will have

$$|\delta_{\mathrm{eff}}^{\mathrm{Doppler}}| = (|\vec{k}_{589\,\mathrm{nm}}| + |\vec{k}_{820\,\mathrm{nm}}|)|v_{\hat{z}}|, \tag{4}$$

where $v_{\hat{z}}$ is the component of the Na I atomic velocity $\vec{v}$ along the laser propagation direction $\hat{z}$. The STIRAP process is highly sensitive to this velocity-dependent detuning δ_{eff}: Na I atoms in the mesosphere that are within the spatial region given by equation (2) and which happen to have a small value of δ_{eff} with respect to pairs of photons from the two lasers will successfully be excited to the $3\,\mathrm{D}_{5/2}$ state via STIRAP, whereas the Na I atoms which do not happen to reside within both this spatial region and this narrow range of velocity along the $\hat{z}$ component direction will fail to be excited via the STIRAP process. The root mean square of the $v_{\hat{z}}$ distribution $v_{\hat{z}}^{\mathrm{RMS}} = \sqrt{\frac{k_B T_{100\,\mathrm{km}}}{M_{\mathrm{Na}}}}$, where $T_{100\,\mathrm{km}} \approx 200$ K, and thus $v_{\hat{z}}^{\mathrm{RMS}} \approx 270$ m s^{-1}. Thus, $\delta_{\mathrm{eff}}^{\mathrm{RMS,\,Doppler}} \approx 4.93 \times 10^9$ s^{-1}. The total effective root mean square detuning $\delta_{\mathrm{eff}}^{\mathrm{RMS}}$ will equal the sum in quadrature of $\delta_{\mathrm{eff}}^{\mathrm{RMS,\,Doppler}}$ and the root mean square linewidths of the lasers (which we will take to each be 1 GHz $= 6.28 \times 10^9$ s^{-1}), and thus $\delta_{\mathrm{eff}}^{\mathrm{RMS}} \approx 1.02 \times 10^{10}$ s^{-1}.

The associated width of the two-photon resonance $\delta_{1/2}$ that corresponds to a STIRAP transition probability of 50 per cent is estimated in Danileiko, Romanenko & Yatsenko (1994) to be given, for Gaussian laser pulses from the two lasers which happen to have equal peak Rabi frequencies, by

$$\delta_{1/2}\sigma_t = A(\Omega_0\sigma_t)^n, \tag{5}$$

where σ_t is the temporal length of the pulses from each of the two lasers; and the peak Rabi frequency $\Omega_0 \equiv \frac{d_{\alpha\beta}\mathcal{E}_0}{2\hbar}$ where $d_{\alpha\beta}$ is the dipole moment between the initial and intermediate state or the intermediate and final state, and $\mathcal{E}_0$ is the peak electric field within the mesosphere of the first laser or the second laser. A and n are both dimensionless, $\mathcal{O}(1)$ constants that are tabulated in Danileiko et al. (1994) and happen to both be approximately equal to 0.9 for the ranges of experimental parameters that we will consider in this paper. We will find in Section 5 that this two-photon resonance width $\delta_{1/2} \ll \delta_{\mathrm{eff}}^{\mathrm{RMS}}$, and specifically that the root mean square detuning $\delta_{\mathrm{eff}}^{\mathrm{RMS}} \approx 1.02 \times 10^{10}$ s^{-1} tends to be around an order of magnitude larger than $\delta_{1/2}$ for the ranges of experimental parameters that we will be considering.

This implies that this two-photon resonance peak (that is parametrized by $\delta_{1/2}$) effectively carves a narrow region of the velocity distribution from the wider Na I detuning spectrum (parametrized by $\delta_{\mathrm{eff}}^{\mathrm{RMS}}$) for STIRAP excitation, and leaves the rest of the sodium atoms within the laser beam column in the mesosphere unexcited. The fraction f_{STIRAP} of the sodium atoms within the column in the mesosphere that happen to be within that narrow region of the velocity distribution will, of course, be proportional to $\frac{\delta_{1/2}}{\delta_{\mathrm{eff}}^{\mathrm{RMS}}}$. To find the constant of proportionality C such that $f_{\mathrm{STIRAP}} = C\frac{\delta_{1/2}}{\delta_{\mathrm{eff}}^{\mathrm{RMS}}}$, we note that if both $\delta_{1/2}$ and $\delta_{\mathrm{eff}}^{\mathrm{RMS}}$ happen to parametrize Gaussian distributions, then $\delta_{\mathrm{eff}}^{\mathrm{RMS}}$ will be equal to 1σ of its Gaussian distribution, whereas $\delta_{1/2}$ is a half-width at half-maximum, i.e. $\sigma\sqrt{2\ln 2}$ of its Gaussian distribution. The value of an integral within a region of width w that is carved from the centre of a broad normal distribution with standard deviation $\sigma \gg w$ is, of course, $\frac{w}{\sigma\sqrt{2\pi}}$. Thus, when the LPRS system happens to be on-centre of the detuning distribution, i.e. at an optimal two-photon laser tuning, the constant of proportionality $C = \frac{1}{\sqrt{2\pi}} \times \frac{1}{\sqrt{2\ln 2}}$, and thus

$$f_{\mathrm{STIRAP}} = \frac{\delta_{1/2}}{2\delta_{\mathrm{eff}}^{\mathrm{RMS}}\sqrt{\pi\ln 2}} \tag{6}$$

under the approximation of Gaussian detuning and two-photon resonance spectra.

Note that various methods such as laser pulse chirping (Pedreros Bustos et al. 2020), or synchronization of pulses (or their polarization) with the Larmor precession of Na I in the geomagnetic field (Kane, Hillman & Denman 2014; Fan, Zhou & Feng 2016; Pedreros Bustos et al. 2018), could potentially be used to, in effect, increase the above ratio, thus potentially increasing LPRS brightness. We do not, however,

assume the implementation of such possible LPRS brightness-increasing techniques in this paper. (We will find in Sections 5–8 that this LPRS will be sufficiently bright that such enhancements should likely not be necessary.)

2.2.2 Signal photon polarization

Another parameter that is relevant, not for the effective rate of STIRAP excitation and resulting emission of the 819.71 and 589.16 nm photons, but rather for the efficiency of their detection by the telescope camera approximately 95 km below, is the polarization of those emitted photons. As mentioned in the previous subsection, the light from the 589.16 and the 819.71 nm lasers will be linearly polarized in the $\hat{x}$- and $\hat{y}$-directions, respectively (and the telescope filters will reject $\hat{x}$-polarized 589.16 nm light and $\hat{y}$-polarized 819.71 nm light, and only accept $\hat{y}$-polarized 589.16 nm light and $\hat{x}$-polarized 819.71 nm light). Due to the fact that the Doppler-broadened linewidth $\frac{\Gamma_{D_f}}{2\pi} \approx 1.5$ GHz is of the same order as, or is significantly greater than, the separations of the hyperfine levels within each of the Na I states i, k, and f that are defined above (where the Doppler linewidth is of the same order for the case of the hyperfine separation within the ground state i, and is significantly greater for the cases of the separations within the excited states k and f), we may safely average over the individual hyperfine levels within each state, when calculating the averaged emitted polarizations of the photons from the sodium layer. Both the 819.71 and the 589.16 nm signal photons that are emitted will be approximately equally polarized in the $\hat{x}$- and $\hat{y}$-directions (i.e. will be nearly unpolarized). A simplified simulation, using the `Atomic Density Matrix` software package (Rochester 2021), of the LPRS system that we describe in this paper shows that there will be a small excess (approximately 0.3 per cent) of 819.71 nm signal photons emitted from the sodium layer that will be polarized in the $\hat{y}$-direction; however, this small excess (and the resulting small deficit in signal photons that successfully pass through the polarized telescope filter) does not significantly affect any of the results of this paper. The necessary addition of linear polarization filters within the telescope's optical filters, in order to filter out what would be an otherwise-dominant atmospheric Rayleigh scattering background does, however, cause the very important loss of just over 50 per cent of signal photons (whether from the LPRS within the upper atmosphere, or from astronomical sources). We include this substantial effect when calculating expected numbers of detected signal photoelectrons in Section 5 of this paper, as well as in subsequent analysis.

2.2.3 Signal excitation to $3\,D_{3/2}$ rather than to $3\,D_{5/2}$

A small fraction of the sodium atom excitations from the pairs of laser pulses will be to the $3\,D_{3/2}$ state, rather than to the $3\,D_{5/2}$ state. This is due to the fact that the $3\,D_{3/2}$ excitation of Na I resides only 1.5 GHz above the intended $3\,D_{5/2}$ excitation and, thus, there will be overlap between these two Na I excitation frequency distributions due to the aforementioned Doppler broadening. Fortunately, the presence of these $3\,D_{3/2}$ excitations in addition to the intended $3\,D_{5/2}$ excitations will not affect the 1:1 ratio of yellow (589/590 nm) photons to near-infrared (819/820 nm) photons from the resulting LPRS, since both the $3\,D_{3/2}$ and $3\,D_{5/2}$ excitations will produce mandated cascades of photons of those two wavelength ranges (the former as shown in fig. 1c in Paper I, and the latter as shown in Fig. 1). These $3\,D_{3/2}$ excitations will be a small subset of the sodium atoms within the column described by equation (2), rather than being within an additional region in excess to it, and thus it is only necessary to consider the total number of sodium atoms in the region described by equation (2), rather than any additional conditions for $3\,D_{3/2}$ excitations.

2.3 Excitation rates of possible significant laser-induced backgrounds other than Rayleigh scattering or virtual $3\,P^*_{3/2}$ excitation production

In addition to the backgrounds described in Section 2.1, two other forms of potentially significant laser-induced background excitation rates, consisting of single-photon and three-photon transition events to the non-virtual $3\,P_{3/2}$ state, per ground-state Na I atom per unit time, will respectively be given by

$$W^{\text{Na I (other bkgd. excitation \#1)}}_{(3\,S_{1/2})+\gamma_{589\,\text{nm}} \rightarrow (3\,P_{3/2})} \approx \frac{\sqrt{\pi}}{4\hbar^2\Gamma_{D_k}} \frac{g_k}{g_i} \left(d_{ik}^2 \mathcal{E}_1^2\right) e^{-\Delta^2/\Gamma_{D_k}^2}, \quad \text{and} \tag{7}$$

$$W^{\text{Na I (other bkgd. excitation \#2)}}_{(3\,S_{1/2})+2\gamma_{589\,\text{nm}} \rightarrow (3\,P_{3/2})+\gamma_{589\,\text{nm}}} \approx \frac{\sqrt{\pi}}{4\hbar^4\Gamma_{D_k}} \frac{g_k}{g_i} \left[\frac{d_{ik}^4 \mathcal{E}_1^4}{\Delta^4}\right] \Gamma_k^2, \tag{8}$$

where d_{ik}, $\mathcal{E}_1$, Δ, Γ_k, $\frac{g_k}{g_i}$, and states i and k are all as defined previously; the Doppler-broadened state k linewidth $\frac{\Gamma_{D_k}}{2\pi} \equiv \frac{\nu_{ki}}{c}\sqrt{\frac{k_B T}{M_{\text{Na}}}} \approx 1$ GHz; and again the approximately equal signs would become exact at their respective orders in perturbation theory in the two equations above if one assumes that the velocity distribution of ground-state Na I atoms within the sodium layer is perfectly Maxwellian, and discounts effects from non-resonant three-photon processes (which are both very good approximations for the ranges of parameters we consider in this paper) (Budker et al. 2008).

A third additional potentially significant laser-induced background rate, consisting of the Lorentzian tail of the distribution of off-resonance transitions to the $3\,P_{1/2}$ state, is

$$W^{\text{Na I (other bkgd. excitation \#3)}}_{(3\,S_{1/2})+\gamma_{589\,\text{nm}} \rightarrow (3\,P_{1/2})} \approx \frac{1}{4\hbar^2} \frac{g_j}{g_i} \left[\frac{d_{ij}^2 \mathcal{E}_1^2}{(\Delta_{3\,P_{1/2}})^2}\right] \Gamma_j, \tag{9}$$

(again, per ground-state Na I atom per unit time) where state $j \equiv 3\,P_{1/2}$; the level degeneracy ratio $\frac{g_j}{g_i} = \frac{2}{2} = 1$; $\Delta_{3\,P_{1/2}} \equiv (3.2414 \times 10^{12}\ s^{-1}) - \Delta$ is the detuning from the $3\,P_{1/2}$ state; the dipole moment $d_{ij} = \sqrt{\frac{3\epsilon_0 \hbar c^3 A_{ji}}{2\omega_{ji}^3}} = 2.10 \times 10^{-29}$ coulomb-metres; and both the Einstein A coefficient A_{ji}, and the natural linewidth Γ_j of state j are equal to $6.14 \times 10^7\ s^{-1}$ (Budker et al. 2008).

Similar to signal photons, the 589.16 nm photons produced from each of these three background processes will be approximately equal mixtures of $\hat{x}$ and $\hat{y}$ linear polarizations, and thus the laser and filter polarizations will not have a significant effect in the cases of these background sources. Nor, unfortunately, will the STIRAP laser pulse shapings and timings affect these three backgrounds. However, as we will calculate in Section 6, the total rates for each of these three backgrounds are fortunately small in comparison with the rate for signal.

As we will find in Section 5, our parameters for the 589.16 and 819.71 nm lasers (which we will provide in more detail in Section 4) would result in an LPRS of 11.9 apparent magnitude in both the r and z filters. And, as we will then calculate in Sections 7 and 8, such an LPRS would have a major impact on the precision of dark energy measurements from SNeIa at the Vera C. Rubin Observatory and at future wide-field SNeIa surveys at other observatories.

3 OTHER LPRS TECHNIQUES WITH DETUNED LASERS CONSIDERED

We have also considered other atomic and molecular excitations that could potentially form upper atmospheric light sources with precise photometric ratios, when utilizing alternative pairs (or triplets) of detuned ground-based lasers. The constraints on properties of atomic systems shown in fig. 2 in Paper I also apply to the properties of atomic systems with detuned lasers that we consider in this paper, with the important exception of constraint 1) that is shown at the bottom of that figure (under the '2-laser option' in that figure). Thus, we have modified the code we used in Paper I, `LPRSAtomicCascadeFinder`,[3] to again search the Kramida et al. (2020) data base, this time for sets of atomic transitions that obey the required constraints on atomic systems with detuned ground-based lasers. In addition to neutral sodium (Na I), we ran this modified `LPRSAtomicCascadeFinder` on the same set of tables of upper-atmospheric atomic species from Kramida et al. (2020) that we considered in Paper I (Al I, C I, Ca I, Fe I, H I, He I, K I, N I, Ne I, O I, Al II, C II, Ca II, Fe II, H II, He II, K II, N II, Na II, Ne II, and O II). The only pair or triplet of atomic transitions that satisfies these required constraints, as coded within the modified `LPRSAtomicCascadeFinder`, is the 589.16 and 819.71 nm transitions of Na I (as shown in Fig. 1 and described in the previous section). We thus believe that Fig. 1 shows the sole upper-atmospheric *atomic* excitation option using a pair (or triplet) of detuned ground-based lasers that meets the required constraints for such systems. In addition, we believe that there are no upper atmospheric *molecular* excitation options (within the optical spectrum) using pairs or triplets of detuned ground-based lasers that could provide viable alternative detuned LPRS systems to the Na I 589.16 and 819.71 nm excitations, either.

4 LASERS AND LAUNCH TELESCOPE

In this section, we provide an example set of specifications and a design outline for two lasers, respectively, tuned to approximately 3.9 GHz below and above the Na I resonances at wavelengths of 589.16 and 819.71 nm, together with a single launch telescope, that would meet the requirements for an LPRS for precision photometric calibration for the case of the Rubin Observatory. Due to the order of magnitude lower average laser output powers required (and the resulting far less stringent demands on the temperature control of internal laser components), these requirements would fortunately be simpler and less costly to engineer than the case of the single 500 W, 342.78 nm laser LPRS that was considered in Paper I.

The maximum optimal laser linewidths σ_ν are determined by the Doppler broadening $\frac{\nu_0}{c}\sqrt{\frac{k_B T}{M_{Na}}}$ of the $3\,D_{5/2}$ excitation ($\nu_0 = 8.75 \times 10^{14}$ Hz) in the upper atmosphere, where $T \approx 200$ K. Thus, the sum of the two laser frequencies should have $\sigma_\nu \lesssim 1.5$ GHz; i.e. if the two lasers have similar linewidths, then they should each optimally have a maximum linewidth of $\sigma_\nu \lesssim (1.5\ \text{GHz})/\sqrt{2} \approx 1$ GHz.

Dye lasers would provide the best performance (i.e. would provide the brightest LPRS with the highest signal-to-background ratio) if one chooses among unmodified and presently commercially available laser source options. However, as solid-state or fibre laser systems generally tend to be more efficient and have lower maintenance requirements than dye laser systems, we outline two possible sets of design options below: (*a*) Dye laser LPRS design options using a pair of pulsed dye lasers that are, respectively, at wavelengths near 589.16 and 819.71 nm; and (*b*) Solid-state/fibre laser LPRS design options using the output of an injection-seeded, Q-switched Nd:YAG laser into a pair of optical parametric oscillator (OPO) crystals, for the generation of pulses at wavelengths near 589.16 and 819.71 nm. As we will show, choices from either one of these sets of design options would be able to meet the requirements for the generation of an LPRS for high-precision photometric calibration.

We first consider the design options (*a*), using a pair of pulsed dye lasers. A pair of dye lasers such as, for example, either a single Sirah Double Dye (Sirah 2021) or a pair of Radiant Dyes NarrowScan High Repetition Rate lasers (Radiant Dyes 2021) can produce pairs of pulses at variable wavelengths, respectively, near 589.16 and 819.71 nm at a repetition rate of 10 kHz, with Gaussian pulses that are each approximately 5 ns FWHM in length (with each 589 nm pulse trailing each 820 nm pulse by approximately 5 ns $\times \frac{1}{2\sqrt{\ln 2}} \approx 3$ ns for implementation of STIRAP). In the case of either the Sirah or the Radiant Dyes lasers, each 589 nm pulse can have approximately 1.5 mJ of energy and each

[3] Available from the authors upon request.

820 nm pulse can have approximately 0.5 mJ of energy (with the 589 nm pulses being approximately a factor of 3 more energetic than the 820 nm pulses because of the approximately 3 × greater efficiency of dyes at 589 nm compared with dyes at 820 nm). The spectral linewidths of the pulses would be $\leq$(0.05 cm^{-1} = 1.5 GHz) in the case of both the 589 and 820 nm output light, when double gratings of approximately (1800–2400) lines per mm are used in each of the dye lasers. In the case of the Sirah Double Dye, the pair of dye lasers would both be pumped by a single Sirah High Repetition Rate Pulsed Amplifier (Sirah 2021) operating at 10 kHz, with its output directed through a high-power polarizing 50:50 beamsplitter cube [such as a CCM1-PBS25-532-HP/M from Thorlabs (2021)], mounted at 45° from the polarization axis of the input laser light. The resulting pairs of linearly polarized pulses (each with $>$ 2000 : 1 extinction ratio between accepted and rejected polarization orientations) would then, respectively, pump the 820 and 589 nm lasers in the Double Dye laser; however, the pump pulses for the 589 nm laser would be time-delayed with respect to the pump pulses from the 820 nm laser by approximately 3 ns by a variable, and approximately (60–120) cm, longer light path, prior to entering the Double Dye lasers, to implement STIRAP. In the case of the pair of Radiant Dyes lasers, the pair of dye lasers would both be pumped by a single EdgeWave IS-series pulsed green laser (EdgeWave 2021) operating at 10 kHz, also with output to a similar polarizing beamsplitter cube, and with the resulting pair of pump pulses also separately delayed so that the pump pulses entering the 589 nm dye laser arrive approximately 3 ns after the pump pulses entering the 820 nm dye laser. Following the pair of either the Radiant Dyes or Sirah dye lasers, the 589 and 820 nm output beams would be recombined (and co-aligned) via a dichroic optic [e.g. product DMLP650L from Thorlabs (2021)]. This recombined beam would then be directed to the launch telescope.

Design options (*b*), which avoid the use of liquid dyes, could be implemented with, for example, a single 532 nm injection-seeded Amplitude Powerlite DLS 9050 frequency-doubled Nd:YAG laser (Amplitude 2021) producing 600 mJ Gaussian pulses that are each approximately 6 ns FWHM in length, with a spectral linewidth of approximately 0.003 cm^{-1} = 90 MHz, at a repetition rate of 50 Hz. Similar to options (*a*) above, the light from this laser would be directed through a polarizing 50:50 beamsplitter cube mounted at 45° from the polarization axis of the input laser light. The two resulting linearly polarized beams would each enter separate lithium triborate (LBO) OPO crystals. The first LBO crystal would be oriented for production of 589.16 nm light (as well as unused 5.48 μm light), and the second LBO crystal would be oriented for production of 819.71 nm light (as well as unused 1.52 μm light). The wavelengths of the two output beams would be variable between, respectively, approximately (589.0–589.2) nm and (819.5–819.8) nm, via small adjustments of the angles of the LBO crystals. The 589 nm pulses would then be time-delayed by approximately 3.6 ns with respect to the 820 nm pulses via an approximately (80–140) cm longer light path of variable length [similar to the time delay in options (*a*) above], to implement STIRAP. The beams would then be recombined and co-aligned via a dichroic optic as in options (*a*) above, and the recombined beam would then be directed to the launch telescope.

The launch telescope would maintain the polarization of the two wavelengths, and expand the combined beam, correspondingly lowering its angular divergence, in order to minimize the resulting beam diameter at 100 km altitude. The launch telescope would have the same general optical design as typical launch telescopes for laser guide stars (LGS), i.e. expansion of the beam to approximately 0.5 m diameter with the minimum achievable wavefront error. Also similar to launch telescopes for LGS (and to the launch telescope considered for the 342.78 nm single-laser LPRS in Paper I): as the laser input to the launch telescope can achieve a beam quality that is within a factor of 2 of diffraction limitation, the resulting output beam from the launch telescope can achieve an angular divergence that is below 0.2 arcsec (the pixel scale of the LSST Camera at the Rubin Observatory).

As in the single-laser LPRS considered in Paper I, the beam diameter at the 100 km altitude of the sodium layer will approximately equal the sum in quadrature of the beam diameter at launch telescope exit (0.5 m), the expansion of the beam in the atmosphere due to its angular divergence at launch telescope exit ($\sim$0.1 m), and the expansion of the beam in the atmosphere due to angular divergence caused by atmospheric turbulence ($\sim$0.5 m); i.e. $\sqrt{(0.5)^2 + (0.1)^2 + (0.5)^2}$ m $\approx$0.7 m, or about 1.4 arcsec on the sky. And furthermore just as in the single-laser LPRS considered in Paper I (as well as also in LGS), a small additional enlargement of the LPRS beam diameter in a radial direction outward from the centre of the telescopic field of view would occur because the centre of the laser launch telescope would be slightly offset from the centre of the aperture of the observing telescope. The LPRS will thus be approximately elliptical in shape on the field of view, with eccentricity of $\sim$0.75 (i.e. the major axis diameter of the LPRS ellipse will be approximately 2.1 arcsec on the sky, with minor axis diameter being the $\sim$1.4 arcsec stated above). Also as in the single-laser LPRS, uncertainties related to flat-fielding of photometric calibration information across the focal plane of the main telescope could be ameliorated by mounting the launch telescope to the outer support structure of the main telescope on a tip-tilt stage, so that the launch telescope could tilt up to $\sim$1° in altitude and azimuth with respect to the main telescope, allowing the LPRS to be moved around the focal plane as needed.

Also as in Paper I, we make the assumption that the laser beam spatial profile will be Gaussian, and additionally that the LPRS profile on the sky will be a Gaussian ellipse. Although the true LPRS profile on the sky will likely have larger tails than a Gaussian distribution, the resulting corrections to the analysis in Sections 5–8 of this paper from a more detailed (and necessarily more complex) parametrization of the LPRS spatial profile would likely be fairly small.

5 ESTIMATION OF OBSERVED LPRS SIGNAL FLUX

We calculate in this section the expected observed flux at an observatory that is located at the same mountaintop site as our presently considered pair of source lasers, and launch telescope, each with properties described in the previous section, from the resulting 589/590 and 819/820 nm light that is generated by the de-excitation of the $3\,D_{5/2}$ (and $3\,D_{3/2}$) states of Na I atoms in the sodium layer. To use equations (2)–(6) to find the total signal excitation rate, we must determine the electric field strengths of the two source laser beams $\mathcal{E}_1$ and $\mathcal{E}_2$ within the altitude range of the sodium layer. The rms electric field strength, in V/m, of an electromagnetic plane wave $\mathcal{E} = \sqrt{240\pi I}$, where I is the instantaneous

intensity in W m^{-2}. The laser pulses each have Gaussian spatial and temporal profiles, so if we were to consider the origin in (x, y, t) to be at the centre of a pulse, then the intensity of that pulse (in W m^{-2}) ,$I(x, y, t) = \frac{E}{(2\pi)^{3/2}\sigma_x\sigma_y\sigma_t} e^{-\frac{1}{2}[(\frac{x}{\sigma_x})^2+(\frac{y}{\sigma_y})^2+(\frac{t}{\sigma_t})^2]}$ where E is the energy of a pulse in joules, t and σ_t are in units of seconds, and (x, σ_x, y, σ_y) are all in units of metres. Per STIRAP, the pulses of the 819.71 nm laser and the 589.16 nm laser will be temporally separated by a time interval τ. Defining $\delta_t \equiv \frac{\tau}{2}$, and centring the origin between pulses from the two lasers, we have that

$$\mathcal{E}_1^2 \;=\; 240\pi I_1 \;=\; \frac{120E_1}{(2\pi)^{\frac{1}{2}}\sigma_x\sigma_y\sigma_t}\mathrm{e}^{-\frac{1}{2}\left[\left(\frac{x}{\sigma_x}\right)^2+\left(\frac{y}{\sigma_y}\right)^2+\left(\frac{t+\delta_t}{\sigma_t}\right)^2\right]},\ \text{and} \tag{10}$$

$$\mathcal{E}_2^2 \;=\; 240\pi I_2 \;=\; \frac{120E_2}{(2\pi)^{\frac{1}{2}}\sigma_x\sigma_y\sigma_t}\mathrm{e}^{-\frac{1}{2}\left[\left(\frac{x}{\sigma_x}\right)^2+\left(\frac{y}{\sigma_y}\right)^2+\left(\frac{t-\delta_t}{\sigma_t}\right)^2\right]}, \tag{11}$$

and thus

$$\int_{x,y,t}\mathcal{E}_1^2\,\mathrm{d}x\,\mathrm{d}y\,\mathrm{d}t \;=\; 240\pi E_1\,, \tag{12}$$

$$\sqrt{d_{ik}^2\mathcal{E}_1^2+d_{kf}^2\mathcal{E}_2^2} \;=\; \sqrt{\frac{120}{(2\pi)^{\frac{1}{2}}\sigma_x\sigma_y\sigma_t}}\mathrm{e}^{-\frac{1}{4}\left[\left(\frac{x}{\sigma_x}\right)^2+\left(\frac{y}{\sigma_y}\right)^2\right]}\sqrt{d_{ik}^2E_1\mathrm{e}^{-\frac{1}{2}\left(\frac{t+\delta_t}{\sigma_t}\right)^2}+\mathrm{d}_{kf}^2E_2\mathrm{e}^{-\frac{1}{2}\left(\frac{t-\delta_t}{\sigma_t}\right)^2}}\,, \tag{13}$$

$$\frac{1}{\hbar}\int_{-\infty}^{\infty}\left(\sqrt{\mathrm{d}_{ik}^2\mathcal{E}_1^2+\mathrm{d}_{kf}^2\mathcal{E}_2^2}\right)\mathrm{d}t \;\approx\; \left(\frac{\pi}{2}\right)^{\frac{1}{4}}\sqrt{\frac{120\sigma_t}{\sigma_x\sigma_y}}\mathrm{e}^{-\frac{1}{4}\left[\left(\frac{x}{\sigma_x}\right)^2+\left(\frac{y}{\sigma_y}\right)^2\right]}\left[\left(1+\Phi\right)\left(\eta_1+\eta_2\right)+\left(1-\Phi\right)\left(\frac{\eta_1^2}{2\eta_2}+\frac{\eta_2^2}{2\eta_1}\right)\right],\ \text{and} \tag{14}$$

$$\int_{x,y,t}\mathcal{E}_1^4\,\mathrm{d}x\,\mathrm{d}y\,\mathrm{d}t \;=\; \frac{7200\sqrt{\pi}E_1^2}{\sigma_x\sigma_y\sigma_t}, \tag{15}$$

where E_1 and E_2 are, respectively, the 589 and the 820 nm laser pulse energies within the mesosphere in joules; $\eta_1 \equiv \frac{d_{ik}\sqrt{E_1}}{\hbar}$ and $\eta_2 \equiv \frac{d_{kf}\sqrt{E_2}}{\hbar}$; $\Phi \equiv \mathrm{erf}(\frac{\delta_t}{2\sigma_t})$, where $\mathrm{erf}(\alpha) \equiv \frac{1}{\sqrt{\pi}}\int_{-\alpha}^{\alpha}\mathrm{e}^{-\beta^2}\mathrm{d}\beta$ is the typical error function; and the approximate equality in equation (14) is due to the use of the approximation[4]

$$\int_{-\infty}^{\infty}\sqrt{\eta_1^2\mathrm{e}^{-\frac{1}{2}\left(\frac{t+\delta_t}{\sigma_t}\right)^2}+\eta_2^2\mathrm{e}^{-\frac{1}{2}\left(\frac{t-\delta_t}{\sigma_t}\right)^2}}\,\mathrm{d}t \;\approx\; \left[\eta_1\int_{-\infty}^{0}\mathrm{e}^{-\frac{1}{4}\left(\frac{t+\delta_t}{\sigma_t}\right)^2}\left(1+\frac{\eta_2^2}{2\eta_1^2}\mathrm{e}^{\frac{\delta_t t}{\sigma_t^2}}\right)\mathrm{d}t\right] + \left[\eta_2\int_{0}^{\infty}\mathrm{e}^{-\frac{1}{4}\left(\frac{t-\delta_t}{\sigma_t}\right)^2}\left(1+\frac{\eta_1^2}{2\eta_2^2}\mathrm{e}^{-\frac{\delta_t t}{\sigma_t^2}}\right)\mathrm{d}t\right]. \tag{16}$$

First, considering the laser design options (*a*) as described in the previous section, we have that the optical energies within each pulse from the source of the 589 and the 820 nm lasers are, respectively, $E_1^{\mathrm{source}} = 1.5$ mJ and $E_2^{\mathrm{source}} = 0.5$ mJ. Similar to typical laser guide star systems, we will assume that ∼70 per cent of that light at each of the two wavelengths is transmitted through the beam transport optics and launch telescope, and projected on to the sky. The atmospheric transmission from the 2663 m Cerro Pachon site up to the mesosphere at wavelengths of ∼589 and ∼820 nm is approximately 90 per cent in the case of both of those wavelengths (with losses dominated by Rayleigh scattering and by water vapour absorption, respectively), and thus,$E_1 = (0.9 \times 0.7 \times E_1^{\mathrm{source}}) = 945$ μJ and $E_2 = (0.9 \times 0.7 \times E_2^{\mathrm{source}}) = 315$ μJ of energy in each pulse, respectively, from the two lasers will arrive at the sodium layer. Since the major and minor axis diameters of the LPRS ellipse are approximately 2.1 and 1.4 arcsec, respectively, at the altitude of the sodium layer these diameters will, respectively, correspond to approximately 1.1 and 0.7 m; and considering the diameters to correspond to $\pm1\sigma$ of their respective 1D Gaussian distributions, we have that $\sigma_x \approx \frac{1.1\,\mathrm{m}}{2} = 0.55$ and $\sigma_y \approx \frac{0.7\,\mathrm{m}}{2} = 0.35$ m. The 5 ns FWHM pulse duration of the lasers corresponds to Gaussian temporal distributions having $\sigma_t \approx 2.1$ ns. Per STIRAP, as discussed in Section 2.1, the temporal separation $\tau = 2\delta_t$ between the pulses will equal $\sqrt{2}\sigma_t$, and thus $\delta_t \approx 1.5$ ns. Thus, per equation (14), we have that the pulse area $\mathcal{A}(x, y) \equiv \frac{1}{\hbar}\int_{-\infty}^{\infty}(\sqrt{d_{ik}^2\mathcal{E}_1^2+d_{kf}^2\mathcal{E}_2^2})\,\mathrm{d}t \;\approx\; 24.9\mathrm{e}^{-\frac{1}{4}[(\frac{x}{0.55\,\mathrm{m}})^2+(\frac{y}{0.35\,\mathrm{m}})^2]}$.

Note that we can now define a 'STIRAP pulse area safety factor' $s_{\mathcal{A}} \equiv \frac{\mathcal{A}_{\max}}{\mathcal{A}_{\min}}$, where $\mathcal{A}_{\min} \equiv 10$ and $\mathcal{A}_{\max}$ is the maximum value of $\mathcal{A}(x, y)$, and thus $s_{\mathcal{A}} \approx 2.49$ here. This 'safety factor' would not directly relate to the brightness of the LPRS, but rather would characterize the degree of concern one might face from the variety of possible imperfections one might face in the construction and setup of the LPRS

[4]An alternative approximation to this integral, such as

$$\int_{-\infty}^{\infty}\sqrt{\eta_1^2\mathrm{e}^{-\frac{1}{2}\left(\frac{t+\delta_t}{\sigma_t}\right)^2}+\eta_2^2\mathrm{e}^{-\frac{1}{2}\left(\frac{t-\delta_t}{\sigma_t}\right)^2}}\,\mathrm{d}t \approx \left[\eta_1\int_{-\infty}^{-\delta_t}\mathrm{e}^{-\frac{1}{4}\left(\frac{t+\delta_t}{\sigma_t}\right)^2}\left(1+\frac{\eta_2^2}{2\eta_1^2}\mathrm{e}^{\frac{\delta_t t}{\sigma_t^2}}\right)\mathrm{d}t\right] + \left[\eta_2\int_{\delta_t}^{\infty}\mathrm{e}^{-\frac{1}{4}\left(\frac{t-\delta_t}{\sigma_t}\right)^2}\left(1+\frac{\eta_1^2}{2\eta_2^2}\mathrm{e}^{-\frac{\delta_t t}{\sigma_t^2}}\right)\mathrm{d}t\right]$$
$$+\left[\mathrm{e}^{-\frac{\delta_t^2}{4\sigma_t^2}}\sqrt{\eta_1^2+\eta_2^2}\int_{-\delta_t}^{\delta_t}\mathrm{e}^{-\frac{t^2}{4\sigma_t^2}}\left(1+\frac{\delta_t^2}{4\sigma_t^4}t^2\right)\mathrm{d}t\right], \tag{16′}$$

or a numerical solution, could be used instead, but each of those result in a $< \pm10$ per cent change in total predicted photon flux from the approximation in equation (16) for all results that we consider.

system: if $s_{\mathcal{A}}$ in the as-built system were to dip below 1, then STIRAP would not take place in the mesosphere, and thus there would be no LPRS generated at all. While an expected value of $s_{\mathcal{A}} \approx 2.49$ for an LPRS might seem reasonably safe, higher values of $s_{\mathcal{A}}$ would, of course, always be preferable, if possible.

Now we must use equations (5) and (6) to determine the excitation fraction $f_{\rm STIRAP}$ of Na I atoms within this mesospheric column that are in the correct velocity range to be excited by the STIRAP process. The width of the two-photon resonance $\delta_{1/2} = A(\Omega_0)^n(\sigma_t)^{n-1}$, where $A \approx n \approx 0.9$, $\sigma_t \approx 2.1$ ns, and $\Omega_0 \approx \frac{d_{ik}}{2\hbar}\sqrt{\frac{120E_1}{\sigma_x\sigma_y\sigma_t\sqrt{2\pi}}} = 1.06 \times 10^9$ s^{-1}, and thus $\delta_{1/2} \approx 8.8 \times 10^8$ s^{-1}. As determined within 2.2.1, the root mean square detuning $\delta_{\rm eff}^{\rm RMS} \approx 1.02 \times 10^{10}$ s^{-1}, and thus $f_{\rm STIRAP} \approx 0.029$.

Multiplying the elliptical cross-section of the mesospheric column by this value of $f_{\rm STIRAP}$, by the 10 kHz rate of pulse pairs from the lasers, and by the column density of approximately 4×10^{13} ground-state Na I atoms per m^2, we have that the total signal excitation (and, thus, total signal de-excitation) rate is

$$2.55 \times 10^{16} \text{ Na I atoms excited per second} \tag{17}$$

in the mesosphere.

Each of those excited Na I atoms will emit one 819/820 nm photon, as well as one 589/590 nm photon, with the photons each emitted in uniform angular distributions. Again, the atmospheric transmission down to the Cerro Pachon site 95 km below is approximately 90 per cent in the case of both of those wavelengths, and thus at the telescope this will correspond to approximately $N_\gamma^{\rm signal} \equiv 0.9 \times (2.55 \times 10^{16}) \times \frac{1}{4\pi\times(9.5\times10^4)^2} =$

$$2.02 \times 10^5 \text{ photons s}^{-1}\text{ m}^{-2} \tag{18}$$

at each of 818.55 or 819.70 nm, and 589.16 or 589.76 nm.

Following the above, and then using an analogous apparent magnitude calculation as in Section 6 of Paper I, we have that

$$m_{\rm AB}^{r\ \rm band} = 11.9, \tag{19}$$

$$m_{\rm AB}^{i\ \rm band} = 12.6, \text{ and} \tag{20}$$

$$m_{\rm AB}^{z\ \rm band} = 11.9 \tag{21}$$

for this LPRS.

If, instead, we consider analogous calculations to the above when using laser design options (*b*) rather than design options (*a*), we obtain an expected signal flux of

$$5.29 \times 10^4 \text{ photons s}^{-1}\text{ m}^{-2} \tag{22}$$

at each of 818.55 or 819.70 nm, and 589.16 or 589.76 nm; and thus apparent magnitudes of

$$m_{\rm AB}^{r\ \rm band} = 13.3, \tag{23}$$

$$m_{\rm AB}^{i\ \rm band} = 14.0, \text{ and} \tag{24}$$

$$m_{\rm AB}^{z\ \rm band} = 13.3 \tag{25}$$

for the LPRS. At first sight, that appears clearly worse (i.e. about a factor of 4 less bright) when compared with laser design options (*a*); however, note that the 'STIRAP pulse area safety factor' $s_{\mathcal{A}}$ that we defined above would be approximately equal to 58.2 for laser design options (*b*), i.e. over 20 times greater than the value of $s_{\mathcal{A}} \approx 2.49$ for laser design options (*a*); and also that both of the two design options appear to be sufficiently bright for use as an LPRS at surveys performed by large telescopes (such as at the Rubin Observatory). Also note that laser design options (*b*) could potentially be made as bright as design options (*a*), without sacrificing their additional safety factor, if the laser pulse repetition rate could be increased significantly beyond 50 Hz. [Analogously, the safety factor $s_{\mathcal{A}}$ could be increased in laser design options (*a*), towards the high value of $s_{\mathcal{A}}$ that is expected in laser design options (*b*), if the energies of the individual dye laser output pulses could be increased significantly.]

Table 1 summarizes the expected numbers of signal photons and resulting observed signal photoelectrons for the case of the Simonyi Survey Telescope at the Rubin Observatory [when using the expected telescope, camera, and filter throughputs as documented in Jones et al. (2019), with unmodified telescope *r*, *i*, and *z* filters], in the cases of either laser design options (*a*) or (*b*). The table rows containing the total numbers of detected LPRS signal photoelectrons, as well as the table rows below them and the analysis in Sections 7 and 8 of this paper, include the important effect of the loss of 55 per cent of the signal photons due to the necessary inclusion of linear polarization filters within the telescope's optical filters to reject Rayleigh-scattered background light.

Similarly to the single-laser LPRS described in Paper I, the dominant systematic uncertainty on the predicted 1:1 ratio between the photon flux at 589/590 nm versus 819/820 nm of this two-laser LPRS would be due to the possibility of inelastic collisions of excited Na I atoms in the mesosphere during the very brief period of atomic de-excitation. However, unlike the single-laser LPRS, this two-laser LPRS has associated background light that will slightly modify the central value of the 1:1 ratio, instead of the expectation value of the ratio being exactly 1:1 and

Table 1. Expected LPRS signal photon flux and photoelectrons collected at the telescope.

Quantity	Expected value for laser design options (*a*)	Expected value for laser design options (*b*)
LPRS signal photon flux at the telescope, at each of 589/590 nm and 819/820 nm	2.02×10^5 photons s^{-1} m^{-2}	5.29×10^4 photons s^{-1} m^{-2}
Total LPRS signal photon collection rate at each of 589/590 nm and 819/820 nm (within the 35 m^2 clear aperture of the Simonyi Survey Telescope at the Rubin Observatory)	7.07×10^6 photons s^{-1}	1.85×10^6 photons s^{-1}
Total number of detected LPRS signal photoelectrons within the elliptical LPRS spot during a 30 s visit	*r* filter: 9.13×10^7 photoelectrons *i* filter:3.82×10^7 photoelectrons *z* filter:5.94×10^7 photoelectrons	2.39×10^7 photoelectrons 1.00×10^7 photoelectrons 1.56×10^7 photoelectrons
Detected signal photoelectrons per 0.2 arcsec × 0.2 arcsec pixel at the centre of the LPRS spot during a 30 s visit	*r* filter:1.52×10^6 photoelectrons *i* filter:6.40×10^5 photoelectrons *z* filter:9.92×10^5 photoelectrons	3.99×10^5 photoelectrons 1.68×10^5 photoelectrons 2.60×10^5 photoelectrons
Signal standard deviation per 0.2 arcsec × 0.2 arcsec pixel at the centre of the LPRS spot during a 30 s visit	*r* filter:1.23×10^3 photoelectrons *i* filter:8.00×10^2 photoelectrons *z* filter:9.96×10^2 photoelectrons	6.32×10^2 photoelectrons 4.10×10^2 photoelectrons 5.10×10^2 photoelectrons

there only being an associated systematic uncertainty on that value. The predicted ratio of photon flux at 589/590 nm versus 819/820 nm, including both its central value modification and its systematic uncertainty, will thus equal $((1 + \delta) \pm \epsilon)$: 1. As we will show in the following Section, the predicted central value modification δ will equal approximately 2.0×10^{-5} for the case of laser design options (*a*). Similarly to the single-laser LPRS, we conservatively estimate the systematic uncertainty on the ratio ϵ to be 9×10^{-5} for this two-laser LPRS.

6 ESTIMATION OF OBSERVED LPRS BACKGROUND

The laser-induced background light associated with this LPRS can be divided into the following six categories:

(1) Background photons from the de-excitations of single-photon transition events of ground-state Na I to the $3\,P_{3/2}$ state (i.e. 'other background excitation #1'), with rate as described by equation (7);

(2) Background photons from the de-excitations of three-photon transition events of ground-state Na I to the $3\,P_{3/2}$ state (i.e. 'other background excitation #2'), with rate as described by equation (8);

(3) Background photons from the de-excitations of two-photon transition events of ground-state Na I to the $3\,P_{1/2}$ state (i.e. 'other background excitation #3'), with rate as described by equation (9);

(4) Background photons from the de-excitations of Na I virtual $3\,P^*_{3/2}$ excitation production, with rate as described by equation (1), that fail to be completely eliminated by both STIRAP and polarization filtering;

(5) Background photons from near-180° atmospheric Rayleigh back-scattering;

(6) Background photons from near-180° atmospheric Raman back-scattering and de-excitation light from other inelastic excitations.

We calculate the expected amount of background light from each of these categories in the following paragraphs. As we will show, background light from category [5] will be the dominant category of laser-induced background light.

6.1 Category [1]

The expected amount of category [1] of laser-induced background light can be calculated using equations (7) and (12). This excitation cross-section, per 589.16 nm laser pulse and per ground-state Na I atom, $\int_{x,y,t}(W^{\text{Na I (other bkgd. excitation \#1)}}_{(3\,S_{1/2})+\gamma_{589\,\text{nm}} \rightarrow (3\,P_{3/2})})\,dx\,dy\,dt \approx$

$(1.03 \times 10^{-6})\ m^2$ in the case of laser design options (*a*), and

$(3.43 \times 10^{-4})\ m^2$ in the case of laser design options (*b*).

Thus, the flux $N^{\text{cat. [1] bkgd.}}_{\gamma}$ at the telescope from this background category will be approximately

$$\left(1.03 \times 10^{-6}\right) \frac{\text{m}^2}{(\text{pulse})(\text{Na I atom})} \times \left(1 \times 10^4\right) \frac{\text{pulses}}{\text{s}} \times \left(4 \times 10^{13}\right) \frac{\text{Na I atoms}}{\text{m}^2} \times \frac{0.9}{4\pi \times (9.5 \times 10^4\ \text{m})^2} = 3.26 \frac{(589\ \text{nm photons})}{\text{s m}^2}$$

for laser design options (*a*), and

$$\left(3.43 \times 10^{-4}\right) \frac{\text{m}^2}{(\text{pulse})(\text{Na I atom})} \times \left(5 \times 10^1\right) \frac{\text{pulses}}{\text{s}} \times \left(4 \times 10^{13}\right) \frac{\text{Na I atoms}}{\text{m}^2} \times \frac{0.9}{4\pi \times (9.5 \times 10^4\ \text{m})^2} = 5.44 \frac{(589\ \text{nm photons})}{\text{s m}^2}$$

for laser design options (*b*).

6.2 Category [2]

We use equations (8) and (15) to calculate the expected amount of background light from category [2]. The cross-section per 589.16 nm laser pulse and per ground-state Na I atom $\int_{x,y,t}(W^{\mathrm{Na\,I\,(other\ bkgd.\ excitation\ \#2)}}_{(3\,S_{1/2})+2\gamma_{589\,\mathrm{nm}}\,\rightarrow\,(3\,P_{3/2})+\gamma_{589\,\mathrm{nm}}})\,\mathrm{d}x\,\mathrm{d}y\,\mathrm{d}t \approx$

$\left(6.19\times10^{-8}\right)$ m^2 in the case of laser design options (*a*), and

$\left(5.68\times10^{-4}\right)$ m^2 in the case of laser design options (*b*).

Thus the flux $N_\gamma^{\mathrm{cat.\,[2]\,bkgd.}}$ at the telescope from this background category will be approximately:

$$\left(6.19\times10^{-8}\right)\frac{\mathrm{m}^2}{(\mathrm{pulse})(\mathrm{Na\ I\ atom})}\times\left(1\times10^{4}\right)\frac{\mathrm{pulses}}{\mathrm{s}}\times\left(4\times10^{13}\right)\frac{\mathrm{Na\ I\ atoms}}{\mathrm{m}^2}\times\frac{0.9}{4\pi\times(9.5\times10^{4}\ \mathrm{m})^2}=0.20\,\frac{(589\ \mathrm{nm\ photons})}{\mathrm{s\,m}^2}$$

for laser design options (*a*), and

$$\left(5.68\times10^{-4}\right)\frac{\mathrm{m}^2}{(\mathrm{pulse})(\mathrm{Na\ I\ atom})}\times\left(5\times10^{1}\right)\frac{\mathrm{pulses}}{\mathrm{s}}\times\left(4\times10^{13}\right)\frac{\mathrm{Na\ I\ atoms}}{\mathrm{m}^2}\times\frac{0.9}{4\pi\times(9.5\times10^{4}\ \mathrm{m})^2}=9.01\,\frac{(589\ \mathrm{nm\ photons})}{\mathrm{s\,m}^2}$$

for laser design options (*b*).

6.3 Category [3]

We use equations (9) and (12) to calculate the expected amount of background light from category [3]. The cross-section per 589.16 nm laser pulse and per ground-state Na I atom $\int_{x,y,t}(W^{\mathrm{Na\,I\,(other\ bkgd.\ excitation\ \#3)}}_{(3\,S_{1/2})+\gamma_{589\,\mathrm{nm}}\,\rightarrow\,(3\,P_{1/2})})\,\mathrm{d}x\,\mathrm{d}y\,\mathrm{d}t \approx$

(4.19×10^{-8}) m^2 in the case of laser design options (*a*), and

(1.40×10^{-5}) m^2 in the case of laser design options (*b*).

Thus, the flux $N_\gamma^{\mathrm{cat.\,[3]\,bkgd.}}$ at the telescope from this background category will be approximately:

$$\left(4.19\times10^{-8}\right)\frac{\mathrm{m}^2}{(\mathrm{pulse})(\mathrm{Na\ I\ atom})}\times\left(1\times10^{4}\right)\frac{\mathrm{pulses}}{\mathrm{s}}\times\left(4\times10^{13}\right)\frac{\mathrm{Na\ I\ atoms}}{\mathrm{m}^2}\times\frac{0.9}{4\pi\times(9.5\times10^{4}\ \mathrm{m})^2}=0.13\,\frac{(589\ \mathrm{nm\ photons})}{\mathrm{s\,m}^2}$$

for laser design options (*a*), and

$$\left(1.40\times10^{-5}\right)\frac{\mathrm{m}^2}{(\mathrm{pulse})(\mathrm{Na\ I\ atom})}\times\left(5\times10^{1}\right)\frac{\mathrm{pulses}}{\mathrm{s}}\times\left(4\times10^{13}\right)\frac{\mathrm{Na\ I\ atoms}}{\mathrm{m}^2}\times\frac{0.9}{4\pi\times(9.5\times10^{4}\ \mathrm{m})^2}=0.22\,\frac{(589\ \mathrm{nm\ photons})}{\mathrm{s\,m}^2}$$

for laser design options (*b*).

6.4 Category [4]

The expected amount of background light from category [4] can be calculated using equations (1) and (12). The cross-section per 589.16 nm laser pulse and per ground-state Na I atom $\int_{x,y,t}(W^{\mathrm{Na\,I\,(bkgd.\ de\text{-}excitation\ during\ pulse,\ if\ no\ STIRAP)}}_{(3\,P^*_{3/2})\,\rightarrow\,(3\,S_{1/2})+\gamma_{589\,\mathrm{nm}}})\,\mathrm{d}x\,\mathrm{d}y\,\mathrm{d}t \approx$

$\left(1.46\times10^{-3}\right)$ m^2 in the case of laser design options (*a*), and

$\left(4.88\times10^{-1}\right)$ m^2 in the case of laser design options (*b*).

However, this is, of course, the cross-section if STIRAP were not used, whereas we are utilizing STIRAP. Thus, we must multiply this without-STIRAP cross-section by the expected small fraction of non-adiabatic losses from the STIRAP process. In well-controlled laboratory experiments, the non-adiabatic loss fraction from STIRAP has been reduced to levels within the range of (10^{-6})–(10^{-8}) using carefully shaped pulses and other optimizations (Vitanov et al. 2017). With our presently considered application of STIRAP from mountaintop-located lasers to the open upper atmosphere of Earth, we conservatively make the assumption of a non-adiabatic loss fraction at the 10^{-4} level, and thus a STIRAP-modified effective cross-section of

$(1.46\times10^{-7})\frac{\mathrm{m}^2}{(\mathrm{pulse})(\mathrm{Na\ I\ atom})}$ in the case of laser design options (*a*), and

$(4.88\times10^{-5})\frac{\mathrm{m}^2}{(\mathrm{pulse})(\mathrm{Na\ I\ atom})}$ in the case of laser design options (*b*).

Thus, we estimate the flux $N_\gamma^{\mathrm{cat.\,[4]\,bkgd.}}$ at the telescope from this background category to be approximately:

$$\left(1.46\times10^{-7}\right)\frac{\mathrm{m}^2}{(\mathrm{pulse})(\mathrm{Na\ I\ atom})}\times\left(1\times10^{4}\right)\frac{\mathrm{pulses}}{\mathrm{s}}\times\left(4\times10^{13}\right)\frac{\mathrm{Na\ I\ atoms}}{\mathrm{m}^2}\times\frac{0.9}{4\pi\times(9.5\times10^{4}\ \mathrm{m})^2}=0.47\,\frac{(589\ \mathrm{nm\ photons})}{\mathrm{s\,m}^2}$$

for laser design options (*a*), and

$$\left(4.88\times10^{-5}\right)\frac{\mathrm{m}^2}{(\mathrm{pulse})(\mathrm{Na\ I\ atom})}\times\left(5\times10^{1}\right)\frac{\mathrm{pulses}}{\mathrm{s}}\times\left(4\times10^{13}\right)\frac{\mathrm{Na\ I\ atoms}}{\mathrm{m}^2}\times\frac{0.9}{4\pi\times(9.5\times10^{4}\ \mathrm{m})^2}\quad=\quad0.78\,\frac{(589\ \mathrm{nm\ photons})}{\mathrm{s\ m}^2}$$

for laser design options (*b*).

6.5 Category [5]

The expected amount of Rayleigh-backscattered laser light that both enter the telescope aperture and is superimposed over the LPRS spot can be calculated using the same technique as in section 7 of Paper I [and specifically using equation (11) in that Section, modified for the different laser wavelengths used in the present paper]. The analogous fractions

$$\begin{aligned}f^{R,\gamma_\lambda}_{b,\text{over LPRS spot}}&\approx\frac{20\pi\times(3.6\times10^{-31})\times(\lambda_\gamma)^{-4.0117}}{3}\int_{z=80000}^{105000}\mathrm{e}^{-\left(\frac{z}{8800}\right)}\mathrm{d}z\int_{\theta=0}^{\tan^{-1}\left(\frac{r}{z-2663}\right)}\sin\theta\,\mathrm{d}\theta\\&\approx7.96\times10^{-14}\ (\text{for}\ \lambda_\gamma=589.16\ \mathrm{nm})\quad\text{and}\quad2.12\times10^{-14}\ (\text{for}\ \lambda_\gamma=819.71\ \mathrm{nm}),\end{aligned}\tag{26}$$

and analogous total numbers of laser photons reaching the mesosphere per second

$$N^{589\,\mathrm{nm\,laser}}_{\gamma_{589\,\mathrm{nm}}}=2.80\times10^{19}\ \text{ and }\ N^{820\,\mathrm{nm\,laser}}_{\gamma_{820\,\mathrm{nm}}}=1.30\times10^{19}\ \text{ in the case of laser design options }(a);\ \text{and}$$

$$N^{589\,\mathrm{nm\,laser}}_{\gamma_{589\,\mathrm{nm}}}=4.67\times10^{19}\ \text{ and }\ N^{820\,\mathrm{nm\,laser}}_{\gamma_{820\,\mathrm{nm}}}=3.90\times10^{19}\ \text{ in the case of laser design options }(b).$$

Thus, the two true fluxes at the telescope from this background category will be

$$f^{R,\gamma_{589\,\mathrm{nm}}}_{b,\text{over LPRS spot}}N^{589\,\mathrm{nm\,laser}}_{\gamma_{589\,\mathrm{nm}}}\approx(2.23\times10^{6})\,\frac{(589\ \mathrm{nm\ photons})}{\mathrm{s\ m}^2};$$

$$f^{R,\gamma_{820\,\mathrm{nm}}}_{b,\text{over LPRS spot}}N^{820\,\mathrm{nm\,laser}}_{\gamma_{820\,\mathrm{nm}}}\approx(2.75\times10^{5})\,\frac{(820\ \mathrm{nm\ photons})}{\mathrm{s\ m}^2}\ \text{in the case of laser design options }(a);$$

$$f^{R,\gamma_{589\,\mathrm{nm}}}_{b,\text{over LPRS spot}}N^{589\,\mathrm{nm\,laser}}_{\gamma_{589\,\mathrm{nm}}}\approx(3.71\times10^{6})\,\frac{(589\ \mathrm{nm\ photons})}{\mathrm{s\ m}^2};$$

$$f^{R,\gamma_{820\,\mathrm{nm}}}_{b,\text{over LPRS spot}}N^{820\,\mathrm{nm\,laser}}_{\gamma_{820\,\mathrm{nm}}}\approx(8.26\times10^{5})\,\frac{(820\ \mathrm{nm\ photons})}{\mathrm{s\ m}^2}\ \text{in the case of laser design options }(b).$$

However, the 589 nm photons from this background category will be predominantly $\hat{x}$-polarized and the 820 nm photons from this background category will be predominantly $\hat{y}$-polarized, and thus they will, respectively, be blocked by the telescope *r* filter (for the 589 nm photons), and by the telescope *i* and *z* filters (for the 820 nm photons). Thus, there are three ways that a photon from this background category could get through the telescope *r*, *i*, or *z* filter:

(1) Imperfect polarization of the output of the lasers, resulting in an admixture of imperfectly polarized photons from the source;
(2) Depolarization of the polarized photons within the atmosphere, either during upward or downward transit; or
(3) Imperfect rejection of properly polarized background photons by the telescope filters.

For (1), the dominant cause of imperfect polarization from the laser source would be from imperfectly polarized output of the polarizing beamsplitter cube. Polarizing beamsplitters such as the CCM1-PBS25-532-HP/M (Thorlabs 2021) that we considered in Section 4 advertise a greater than 1000:1 ratio between accepted and rejected polarizations, so we conservatively estimate at the bottom of this range, i.e. a $\frac{1}{1000}$ admixture of incorrectly polarized photons from the laser sources. For (2), typical depolarization fractions of a laser beam following a vertical path through the Earth's atmosphere are in the range of (1×10^{-7})–(5×10^{-5}) (Höhn 1969), thus this effect would be relatively negligible. For (3), the rejection of properly polarized background photons would be implemented using a polarizing filter, which should have a greater than 1000:1 ratio between accepted and rejected polarizations. Again, we conservatively estimate at the bottom of this range, and thus we estimate that $\frac{1}{1000}$ of incident properly polarized photons will manage to pass through the telescope filters. The combination of (1), (2), and (3) will approximately result in the sum of the three effects, and thus the true fluxes from this background category should be multiplied by a factor of approximately $\frac{1}{1000}+\frac{1}{1000}=\frac{1}{500}$ due to the rejection of properly polarized photons from this background category in order to obtain the resulting effective fluxes.

Thus, the effective fluxes at the telescope from this background category will be approximately:

$$\frac{1}{500}\times f^{R,\gamma_{589\,\mathrm{nm}}}_{b,\text{over LPRS spot}}N^{589\,\mathrm{nm\,laser}}_{\gamma_{589\,\mathrm{nm}}}\approx(4.46\times10^{3})\,\frac{(589\ \mathrm{nm\ photons})}{\mathrm{s\ m}^2}$$

and

$$\frac{1}{500}\times f^{R,\gamma_{820\,\mathrm{nm}}}_{b,\text{over LPRS spot}}N^{820\,\mathrm{nm\,laser}}_{\gamma_{820\,\mathrm{nm}}}\approx(5.50\times10^{2})\,\frac{(820\ \mathrm{nm\ photons})}{\mathrm{s\ m}^2}$$

in the case of laser design options (*a*); and

$$\frac{1}{500}\times f^{R,\gamma_{589\,\mathrm{nm}}}_{b,\text{over LPRS spot}}N^{589\,\mathrm{nm\,laser}}_{\gamma_{589\,\mathrm{nm}}}\approx(7.42\times10^{3})\,\frac{(589\ \mathrm{nm\ photons})}{\mathrm{s\ m}^2}$$

and

$$\frac{1}{500} \times f_{b,\text{over LPRS spot}}^{R,\gamma_{820\,\text{nm}}} N_{\gamma_{820\,\text{nm}}}^{820\,\text{nm laser}} \approx (1.65 \times 10^3) \frac{(820\,\text{nm photons})}{\text{s m}^2}$$

in the case of laser design options (*b*).

This seems like it would result in a major problem, since these fluxes from this background category are a significant fraction of the expected signal fluxes from equations (18) and (22), even after the above small wrong-polarization acceptance factor of approximately $\frac{1}{500}$ for this background is included. However, unlike background from categories [1] to [4], the Rayleigh-scattered background will not be superimposed purely on the LPRS spot, but rather will form a continuous streak, as was discussed in section 7 of Paper I; and thus one is able to perform a combined fit to the Rayleigh streak as a continuous (and approximately exponentially falling) distribution within the telescope camera images, together with a fit to the LPRS spot that rests on top of the tail of that continuous distribution. This fit technique will be discussed further, and demonstrated, in the following Section on expected photometric ratio precision. One is, thus, still able to achieve high precision on the observationally fitted photometric ratio.

6.6 Category [6]

Similarly to the case of the 342.78 nm laser in Paper I, the atmospheric Raman backscattering of light from the 589.16 and 819.71 nm lasers in the present paper would contribute to the observed LPRS background. However, just as in Paper I, the largest such background contributions would be from the strong Raman lines in the Schumann–Runge bands of O_2, which will produce cross-sections only of order 10^{-40} cm^2 per molecule, and are thus also negligible here.

As also noted in Paper I, the maximum line intensity of O_2 and N_2 Raman rotational transitions corresponding to the first vibrational excitation in these molecules is approximately 10^{-16} erg s^{-1} cm^{-2} (Calia et al. 2014; Vogt et al. 2017). That value is negligible when compared with the returned signal flux from the sodium layer, which will have an intensity at 589.16/589.76 nm calculated in Section 5 of this paper of approximately 7×10^{-11} erg s^{-1} cm^{-2} in the case of laser design options (*a*), and approximately 2×10^{-11} erg s^{-1} cm^{-2} in the case of laser design options (*b*).

6.7 Total laser-induced background

The laser-induced backgrounds from the six different categories will all interfere with one another, and thus one must consider their relative phases in order to add them. However, in practice, the contributions from the different background categories will not be coherent with one another over timescales longer than at most a few tens of nanoseconds, and in any case the background from category [5] greatly dominates over the other categories; thus one can approximate the total laser-induced background either by the incoherent sum of light from the six categories, or by just the light from category [5]; those two methods produce essentially the same result. Thus, we estimate the total effective laser-induced background fluxes from within the 2.1 arcsec × 1.4 arcsec diameter LPRS ellipse to be $(4.5 \times 10^3) \frac{(589\,\text{nm photons})}{\text{s m}^2}$ and $(5.5 \times 10^2) \frac{(820\,\text{nm photons})}{\text{s m}^2}$ in the case of laser design options (*a*); and $(7.4 \times 10^3) \frac{(589\,\text{nm photons})}{\text{s m}^2}$ and $(1.7 \times 10^3) \frac{(820\,\text{nm photons})}{\text{s m}^2}$ in the case of laser design options (*b*).

However, as noted above, the dominant background from category [5] is of a different nature than the other background categories, in that it will form a continuous streak within each image; and thus one can perform an image-by-image combined fit for category [5] background as well as for signal. Whereas the background from other categories, with effective fluxes that per our estimations will sum to a total of $N_\gamma^{\text{peaking bkgd.}} \equiv \sum_{i=1}^{4} N_\gamma^{\text{cat. [}i\text{] bkgd.}} = 4.04 \frac{(589\,\text{nm photons})}{\text{s m}^2}$ in the case of laser design options (*a*) and $15.45 \frac{(589\,\text{nm photons})}{\text{s m}^2}$ in the case of laser design options (*b*), will be superimposed on the LPRS spot; and thus one must use other techniques besides image-by-image fitting – for example, multiple-image scans with variation of the laser detuning parameter Δ, and/or of the relative intensities, and/or pulse shapes, of the two lasers – to experimentally determine those fluxes. We additionally note that the expected central value modification δ on the 1:1 ratio between the photon flux at 589/590 nm versus 819/820 nm that was mentioned at the end of Section 5 will equal $(N_\gamma^{\text{peaking bkgd.}})/(N_\gamma^{\text{signal}}) = \frac{4.04}{2.02 \times 10^5} = 2.0 \times 10^{-5}$ in the case of laser design options (*a*), and $\frac{15.45}{5.29 \times 10^4} = 2.9 \times 10^{-4}$ in the case of laser design options (*b*); where N_γ^{signal} is the signal photon flux from equation (18) in the case of laser design options (*a*), and from equation (22) in the case of laser design options (*b*).

6.8 Non-laser-induced backgrounds

In addition to the above total amount of laser-induced background light calculated in the previous paragraphs, there will also be the typical diffuse sky background (including all other [i.e. non-laser] light that is scattered by the optical elements of the telescope, by the atmosphere, and by zodiacal dust), as well as instrumental background noise. These sources of diffuse background will be corrected through the usual technique of sky subtraction. The amount of diffuse sky background at the Rubin Observatory site is estimated in Jones (2017) to be, for the *r*, *i*, and *z* filters, respectively:

(i) An apparent magnitude per square arcsecond of 21.2, 20.5, and 19.6;
(ii) 42.8, 61.5, and 101.3 $\frac{\text{photons}}{\text{s m}^2\ \text{(square arcsecond)}}$;
(iii) 1498, 2151, and 3544 photons/s/(square arcsecond) (within the 35 m^2 clear aperture of the Simonyi Survey Telescope at the Rubin Observatory);

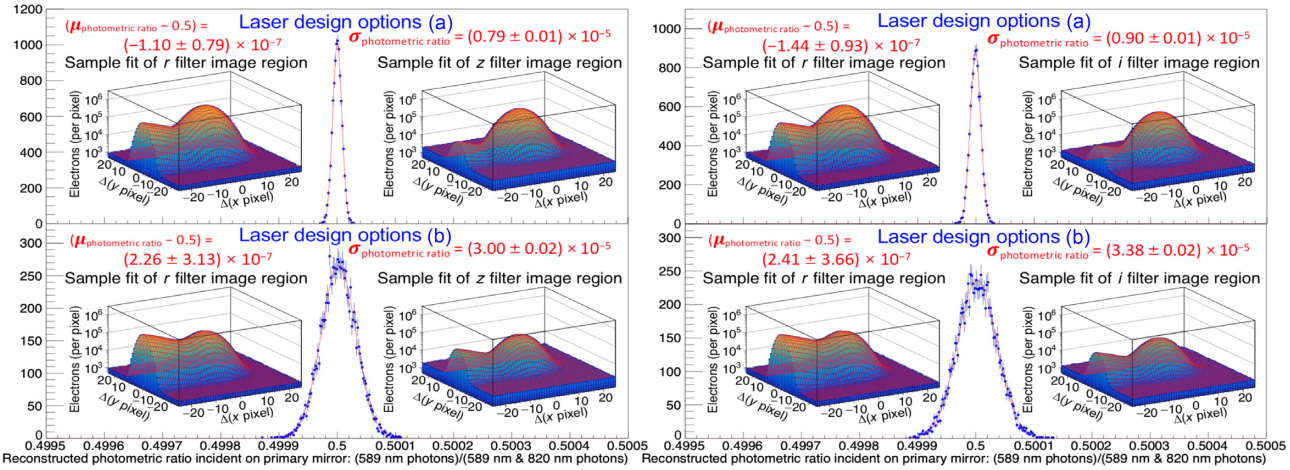

Figure 2. Within each of the four sets of plots above, the main plot (i.e. the one-dimensional fitted Gaussian curve in the centre of each set of plots) shows the distribution of 10000 fitted photometric ratios, with each ratio reconstructed from pairs of simulated *r* and *z* filter image regions (within the two sets of plots on the left-hand side above), and pairs of simulated *r* and *i* filter image regions (within the two sets of plots on the right-hand side above). Within both the left-hand and right-hand sets of plots, the upper set of plots shows the results of fits with image regions simulated when assuming that the LPRS is generated with laser design options (*a*), with specifications detailed in Section 4; and the lower set of plots shows the results when assuming that the LPRS is instead generated with laser design options (*b*). Within each of the four sets of plots, each one of the respective 2 × 10 000 simulated image regions consists of a 50 pixel × 50 pixel square centred around the observed LPRS centroid. The inset plots show single examples of simulated *r*- and *z*-image regions (within the two sets of plots on the left), and simulated *r*- and *i*-image regions (within the two sets of plots on the right), with their respective fits to two-dimensional Gaussian LPRS signal ellipses, plus the product of a falling exponential along the *x*-axis and a Gaussian distribution along the *y*-axis to parametrize the tail of the trail of Rayleigh-scattered background laser light that 'leads up' to the LPRS spot (which is perhaps reminiscent of an 'entrance to an igloo' in all of the inset plots), plus flat background distributions. These inset plots all have a logarithmic *z*-axis, and linear *x*- and *y*-axes. The simulated signal photoelectrons, Rayleigh background photoelectrons, and sky + noise background photoelectrons, in each simulated pixel within each region, are generated according to the statistical distributions expected from a single 30 s LSST visit consisting of a pair of 15 s exposures. The fitted number of signal photoelectrons is extracted from each image region fit, and divided by the (photoelectron)/(incident photon) efficiency (consisting of the expected LSST detector quantum efficiency, multiplied by the expected throughput fraction of telescope, camera, and filter optics, at 589 nm and at 820 nm for the simulated *r*, *z*, and *i* filter image regions, respectively), to determine the reconstructed numbers of 589 nm and 820 nm photons incident on the Rubin Observatory primary mirror during the 30 s visit. For each simulated image region pair, the resulting ratio of reconstructed (589 nm photons)/(589 nm photons + 820 nm photons) is plotted, and the resulting distribution is fitted to a single Gaussian. The standard deviations of the fits shown in the main plots within the two *left* sets of plots above, which correspond to the expected LPRS photometric ratio statistical uncertainties from a single pair of visits with the *r* and *z* filter, are equal to $(0.79 \pm 0.01) \times 10^{-5}$ in the case of an LPRS that is generated according to laser design options (*a*), and to $(3.00 \pm 0.02) \times 10^{-5}$ in the case of an LPRS that is generated according to laser design options (*b*). The standard deviations of the fits shown in the main plots within the two *right* sets of plots above, which correspond to the expected LPRS photometric ratio statistical uncertainties from a single pair of visits with the *r* and *i* filter, are equal to $(0.90 \pm 0.01) \times 10^{-5}$ in the case of an LPRS that is generated according to laser design options (*a*), and to $(3.38 \pm 0.02) \times 10^{-5}$ in the case of an LPRS that is generated according to laser design options (*b*). The means of the fits that are shown in the main plots within all four of these sets of plots are all consistent with 0.5.

(iv) 3459, 5141, and 8472 photons/s from within the elliptical LPRS spot of angular diameter 2.1 arcsec × 1.4 arcsec;

(v) Total numbers of observed sky background photoelectrons equal to 4.46×10^4, 6.63×10^4, and 1.07×10^5 within the elliptical spot during a 30 s visit;

(vi) 747, 1110, and 1701 photoelectrons per 0.2 arcsec × 0.2 arcsec pixel during a 30 s visit; and

(vii) Standard deviations due to the sky background of approximately $\sqrt{747} = 27.3$, $\sqrt{1110} = 33.3$, and $\sqrt{1701} = 41.2$ photoelectrons per pixel per visit.

Within the same 30 s visit time interval, the expected standard deviation in each pixel, in each filter, due to instrumental background noise is 12.7 photoelectrons (Jones 2017).

7 RESULTING ESTIMATED PHOTOMETRIC RATIO PRECISION

Fig. 2 shows the results of sets of numerical simulations to determine the precision of photometric ratio measurement when using single pairs of 30 s LSST visits to the LPRS spot. As shown in Fig. 2, for pairs of visits in the *r* and *z* filters, the resulting estimates of the photometric ratio measurement and its statistical uncertainty are $0.5 \pm (0.79 \times 10^{-5})$ for the case of an LPRS generated using laser design options (*a*), and $0.5 \pm (3.00 \times 10^{-5})$ for the case of an LPRS generated using laser design options (*b*); and for pairs of visits in the *r* and *i* filters, the resulting estimates of the photometric ratio measurement and its statistical uncertainty are $0.5 \pm (0.90 \times 10^{-5})$ for the case of an LPRS generated using laser design options (*a*), and $0.5 \pm (3.38 \times 10^{-5})$ for the case of an LPRS generated using laser design options (*b*).

This shows that in the case of either laser design options (*a*) or (*b*), one can reach the expected systematic uncertainty limit on the LPRS photometric ratio [which is estimated as $\pm(9.0 \times 10^{-5})$, as stated at the end of Section 5] by utilizing the LPRS together with just a single pair of 30 s LSST visits either in the *r* and *z* filters, or in the *r* and *i* filters.

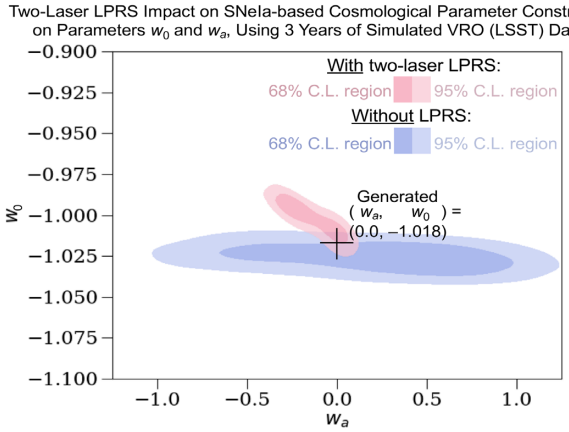

Figure 3. Constraints on the dark energy equation of state parameters w_0 and w_a, obtained using simulated catalogues of type Ia supernovae. Each one of the two SNeIa catalogues that are fitted to obtain these constraints contains 120 000 simulated SNeIa (corresponding to approximately 3 yr of observation at the Rubin Observatory). The generation of the two simulated SNeIa catalogues, as well as the fits that are performed to each catalogue, are implemented using the `CosmoSIS` cosmological parameter estimation code (Zuntz et al. 2015), and are explained in the text here, as well as in section 9 of Paper I. The resulting values of the figure of merit parameter $\mathcal{F}_{\rm DE}$ for the fits are 313 for the fit to the SNeIa catalogue representing expected LSST observations without LPRS-based photometric calibration, and 1646 for the fit to the SNeIa catalogue representing expected LSST observations with photometric calibration from the two-laser LPRS described in this paper. (Also, as would be expected on average, the central values of each fit are approximately one standard deviation away from the generated values of w_0 and w_a.) The fits represent a $\frac{1646}{313} = 5.26$-fold expected improvement in the dark energy figure of merit parameter $\mathcal{F}_{\rm DE}$ from LPRS-based photometric calibration (with even greater expected resulting $\mathcal{F}_{\rm DE}$ increases for SNeIa datasets that correspond to greater than 3 yr of Rubin Observatory observation).

8 ESTIMATED IMPACT ON MEASUREMENTS OF DARK ENERGY FROM TYPE IA SUPERNOVAE

We estimate the impact on the precision of upcoming measurements of the dark energy equation of state as a function of redshift, $w(z)$, from the photometric ratio calibration provided by this LPRS. Our analysis proceeds in an analogous way to the impact analysis that is described in section 9 of Paper I. In particular, we also use the typical parametrization $w(z) = w_0 + \frac{z}{1+z} w_a$ here (where the quantities w_0 and w_a, respectively, parametrize the equation of state of dark energy at the present time, and the amount of change in the equation of state of dark energy over cosmic history). And again we use the typical figure of merit $\mathcal{F}_{\rm DE} \equiv [\det \mathbf{C}(w_0, w_a)]^{-\frac{1}{2}}$, where $\mathbf{C}(w_0, w_a)$ is the covariance matrix of the (w_0, w_a) estimations, to characterize the expected performance of a measurement of the properties of dark energy.

We additionally use a nearly identical procedure to that described in section 9 of Paper I, in order to generate the simulated data set catalogue of SNeIa that represents the expected LSST observations with the photometric calibration that would result from the LPRS described in this paper. The sole differences in the catalogue generation here are from the larger expected improvements in the SNeIa apparent magnitude uncertainties that would result from the two-laser LPRS that is described in this paper:

(i) When generating the simulated SNeIa catalogue that represents expected LSST observations with LPRS-based photometric calibration, the generated systematic uncertainties on the SNeIa magnitudes are reduced by a factor of 4.01 from those in the joint light-curve analysis (JLA) that is described in Betoule et al. (2014), corresponding to the expected improvement in SNeIa magnitude measurement from photometric calibration from this LPRS;

(ii) Also when generating the simulated SNeIa catalogue that represents expected LSST observations with photometric calibration from this LPRS, the generated systematic covariances between the SNeIa magnitude and light-curve stretch values, as well as between the SNeIa magnitude and colour parameter values, are similarly reduced by a factor of 2.00 from those in the JLA, corresponding to the expected improvement in SNeIa magnitude measurement from this LPRS-based photometric calibration.

An identical catalogue to that used in the analysis described in section 9 of Paper I is used to represent expected LSST observations without LPRS-based photometric calibration. And, an identical fitting strategy to the one that is described in that Section is used here for the fits to both simulated SNeIa catalogues.

The results of the fits to the two simulated catalogues, when projected on to the (w_0, w_a) plane (and, thus, when marginalized over all of the other fitted parameters), are shown in Fig. 3. The resulting values of the figure of merit parameter $\mathcal{F}_{\rm DE}$ for the fits are 313 for the fit to the SNeIa catalogue representing expected LSST observations without LPRS-based photometric calibration, and 1646 for the fit to the SNeIa catalogue representing expected LSST observations with LPRS-based photometric calibration, representing a $\frac{1646}{313} = 5.26$-fold expected improvement in the dark energy figure of merit parameter $\mathcal{F}_{\rm DE}$ from photometric calibration from this LPRS over 3 yr of Rubin Observatory observation. (Even larger resulting $\mathcal{F}_{\rm DE}$ increases due to this LPRS-based photometric calibration would be expected for SNeIa data sets that correspond to greater than 3 yr of Rubin Observatory observation.)

9 CONCLUSIONS AND COMPARISON OF LPRS TECHNIQUES

In this paper, together with Paper I, we present two methods for establishing a reference for relative photometry between the visible and NIR (and specifically between photometry at 589/590 nm and 819/820 nm wavelengths) of unprecedented precision using mountaintop-located laser sources to excite neutral atoms of sodium in the mesospheric sodium layer. The method that is described in Paper I would utilize a single laser tuned to the 342.78 nm excitation wavelength of neutral atomic sodium, and would require this laser to have very high ($\geq$500 W) optical output power; whereas the method that is described in this paper would utilize two lasers, respectively tuned to 3.9 GHz below and above the neutral sodium resonances at 589.16 and 819.71 nm wavelengths, and would permit much lower laser optical output power (within a 10–30 W output power range that is available with some present off-the-shelf dye laser systems). The method that is described in this paper would, however, require new polarization filters to be installed into the telescope camera in order to sufficiently remove laser atmospheric Rayleigh backscatter from the resulting telescope images.

As we have shown in this paper, when implemented this method described here will improve measurements of dark energy from type Ia supernovae, using upcoming surveys such as the first 3 yr of observations at the Rubin Observatory, by approximately a factor of 5.26 for the standard dark energy 'figure of merit' $\mathcal{F}_{\rm DE}$ (which is based on the expected uncertainties on measurements of the dark energy equation of state parameters w_0 and w_a). The LPRS technique that is described in this paper, when compared with the technique described in Paper I, would provide a far greater improvement in the measurements of these dark energy parameters, due to the fact that the resulting LPRS would be over a factor of 10^3 brighter than the LPRS described in Paper I, thus in effect removing limitations from observed LPRS photon statistics. (And also, we note, could be continuously dimmed down across that full range of brightness, for use in testing of the linearity of the relative photometry.) Additionally, the two-laser LPRS described in this paper would be far less challenging and expensive to construct than the one-laser LPRS that is described in Paper I, due to the much lower required optical output power of the two lasers, when compared with the output power required of the single-laser LPRS. Thus, we prefer and recommend the development and testing of the two-laser LPRS that is described in this paper. (We must also note that if time and cost were no issue, one would, of course, prefer the development and testing of both options, especially since the one-laser LPRS does have an interesting comparative advantage of not requiring polarization filters to be installed in the telescope camera. However, given the choice, the two-laser LPRS would be, by far, the simpler and more effective option of the two.)

The two-laser LPRS that is described in this paper uses the STIRAP (STImulated Raman Adiabatic Passage) process to excite mesospheric neutral sodium atoms. STIRAP is a well-established technique developed 30 years ago, and demonstrated in thousands of results in laboratories across the world that have been documented in over 200 publications and multiple review articles since 1990 [as examples, Bergmann et al. (2015), and Vitanov et al. (2017)]; however, the STIRAP technique has not yet been demonstrated in the open atmosphere. Thus, this will be a novel challenge; however, when complete, the implementation of this two-laser LPRS may thus mark the first utilization and observation of 'STIRAP in the sky' – an important milestone in the progress of the STIRAP technique, in addition to the specific usage of this LPRS for calibration of unprecedented precision in cosmology, astronomy, and atmospheric physics.

ACKNOWLEDGEMENTS

The authors would like to thank Prof. Gabriele Ferrari of Università di Trento and of LEOSolutions (Rovereto, Italy) for critical and useful discussions regarding parametric crystal options for laser wavelength tunability. The authors appreciate the encouragement by Prof. Christopher Stubbs of Harvard University during the early stage work on both papers. We would also like to thank Dr. Andrew MacRae of the University of Victoria for reading over the manuscript and providing extremely helpful comments and suggestions. JEA gratefully acknowledges support from Canadian Space Agency grants 19FAVICA28 and 17CCPVIC19.

DATA AVAILABILITY

All code and data generated and used for the results of this paper is available from the authors upon request.

REFERENCES

Albert J. E. et al., 2021, MNRAS, submitted (Paper I)
Amplitude Laser Group (Pessac, France), 2021, Product Powerlite DLS 9050 Laser. https://amplitude-laser.com/wp-content/uploads/2019/02/Powerlite-DLS-9 000_ref-f_BD.pdf
Bergmann K., Vitanov N. V., Shore B. W., 2015, J. Chem. Phys., 142, 170901
Betoule M. et al., 2014, A&A, 568, A22
Budker D., Kimball D. F., DeMille D. P., 2008, Atomic Physics: An Exploration Through Problems and Solutions, 2nd edn. Oxford Univ. Press, Oxford
Calia D. B., Hackenberg W., Holzlöhner R., Lewis S., Pfrommer T., 2014, Adv. Opt. Technol., 3, 345
Connor T. et al., 2017, ApJ, 848, 37
Danileiko M. V., Romanenko V. I., Yatsenko L. P., 1994, Opt. Commun., 109, 462
EdgeWave GmbH (Würselen, Germany), 2021, Product nos. ISxxx-2 green IS-series Lasers. https://www.edge-wave.de/web/wp-content/uploads/ISweb.pdf
Fan T., Zhou T., Feng Y., 2016, Sci. Rep., 6, 19859
Gaubatz U. et al., 1990, J. Chem. Phys., 92, 5363
Höhn D. H., 1969, Appl. Opt., 8, 367

Johnson J. B. et al., 2010, Proc. SPIE Conf. Ser. Vol. 7665, STIRAP on Sodium Gas as a Function of Argon Buffer Gas Pressure in Chemical, Biological, Radiological, Nuclear, and Explosives (CBRNE) Sensing XI. SPIE, Bellingham, p. 766512
Jones L., 2017, Technical Report, 'Calculating LSST Limiting Magnitudes and SNR'. LSST/VRO Simulation Technical Note 002 (SMTN-002). https://smtn-002.lsst.io
Jones D. O. et al., 2018, ApJ, 857, 51
Jones L. et al., 2019, Systems Engineering-approved LSST Throughputs Repository. https://github.com/lsst-pst/syseng_throughputs
Kane T. J., Hillman P. D., Denman C. A., 2014, in Proc. SPIE Conf. Ser. Vol. 9148, Adaptive Optics Systems IV. SPIE, Bellingham, p. 91483G
Kelleher D. E., Podobedova L. I., 2008, J. Phys. Chem. Ref. Data, 37, 267
Kirk D. et al., 2015, MNRAS, 451, 4424
Kramida A., et al., 2020, Technical Report, Atomic Spectra Database (Version 5.8). NIST, https://physics.nist.gov/asd
Laser GmbH (Wermelskirchen, Germany), 2021, product NarrowScan High Rep. Laser. https://www.radiant-dyes.com/PDF/6_NarrowScan20high20Rep_Juni202011.pdf
Pedreros Bustos F. et al., 2018, Nat. Commun., 9, 3981
Pedreros Bustos F. et al., 2020, J. Opt. Soc. Am. B, 37, 1208
Rochester S. M., 2021, The Atomic Density Matrix Software Package Can be Downloaded from http://rochesterscientific.com/ADM/; and was initially described in Rochester, S. M. 'Modeling Nonlinear Magneto-optical Effects in Atomic Vapors' Ph.D. dissertation, 2010. University of California, Berkeley
Sirah, 2021, Lasertechnik GmbH (Grevenbroich, Germany), product Double Dye Laser. http://www.sirah.com/wp-content/uploads/documents/DoubleDye.pdf; and product Pulsed Amplifier 2xHRR, http://www.sirah.com/wp-content/uploads/2021/03/PulsedAmp-2xHRR.pdf
Thorlabs, 2021, Inc. (Newton, NJ, USA), product no. CCM1-PBS25-532-HP/M. https://www.thorlabs.com/thorproduct.cfm?partnumber = CCM1-PBS25-532-HP/ M; and product no. DMLP650L, https://www.thorlabs.com/thorproduct.cfm?partnumber = DMLP650L
Vitanov N. V. et al., 2017, Rev. Mod. Phys., 89, 015006
Vogt F. P. A. et al., 2017, Phys. Rev. X, 7, 021044
Wood-Vasey W. M. et al., 2007, ApJ, 666, 694
Zuntz J. et al., 2015, Astron. Comput., 12, 45 (with code repository and instructions available at https://bitbucket.org/joezuntz/cosmosis/wiki/Home)

This paper has been typeset from a TEX/LATEX file prepared by the author.